

**AD-A237 759**



ONR41  
LTR-91-009

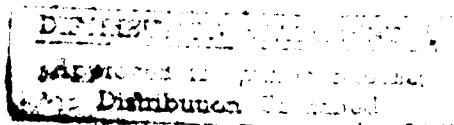
Final Report  
**DEVELOPMENT OF  
OPTICAL SUBAPERTURES**



Prepared by:  
David E. B. Lees  
Norman R. Guivens, Jr.  
Philip D. Henshaw

Prepared for:  
Office of Naval Research  
Code N00014  
800 N. Quincy Street  
Arlington, VA 22217-5000

Contract No. N00014-90-C-0199



17 June 1991

"Research supported by the Strategic Defense Initiative/Innovative Science and Technology and managed by the Office of Naval Research."

**DISCLAIMER**

The views, opinions, and/or findings contained in this report are those of the authors, and should not be construed as an official position, policy, or decision of either the Strategic Defense Initiative/Innovative Science and Technology Organization or the Office of Naval Research unless so designated by other official documentation.

SPARTA, Inc.  
24 Hartwell Avenue  
Lexington, MA 02173  
(617) 863-1060

**91-03178**



UNCLASSIFIED

SECURITY CLASSIFICATION OF THIS PAGE

## REPORT DOCUMENTATION PAGE

1a. REPORT SECURITY CLASSIFICATION UNCLASSIFIED			1b. RESTRICTIVE MARKINGS	
2a. SECURITY CLASSIFICATION AUTHORITY			3. DISTRIBUTION / AVAILABILITY OF REPORT	
2b. DECLASSIFICATION / DOWNGRADING SCHEDULE				
4. PERFORMING ORGANIZATION REPORT NUMBER(S) LTR91-009			5. MONITORING ORGANIZATION REPORT NUMBER(S)	
6a. NAME OF PERFORMING ORGANIZATION SPARTA, INC.		6b. OFFICE SYMBOL (If applicable)	7a. NAME OF MONITORING ORGANIZATION OFFICE OF NAVAL RESEARCH	
6c. ADDRESS (City, State, and Zip Code) 24 HARTWELL AVENUE LEXINGTON, MA 02173			7b. ADDRESS (City, State, and Zip Code) CODE N00014 800 N. QUINCY STREET ARLINGTON, VA 22217-5000	
8a. NAME OF FUNDING / SPONSORING ORGANIZATION SDIO		8b. OFFICE SYMBOL (If applicable)	9. PROCUREMENT INSTRUMENT IDENTIFICATION NUMBER N00014-90-C-0199	
8c. ADDRESS (City, State, and Zip Code) WASHINGTON, DC 20301-7100			10. SOURCE OF FUNDING NUMBERS	
			PROGRAM ELEMENT NO.	PROJECT NO. 126
11. TITLE (Include Security Classification) DEVELOPMENT OF OPTICAL SUBAPERTURES				
12. PERSONAL AUTHOR(S) David E.B. Lees, Norman R. Guivens, Jr., and Philip D. Henshaw				
13. TYPE OF REPORT FINAL		13b. TIME COVERED FROM 09/01/90 TO 02/28/91		14. DATE OF REPORT (Year, Month, Day) 51 JUNE 17
15. PAGE COUNT 49				
16. SUPPLEMENTARY NOTATION				
17. COSATI CODES			18. SUBJECT TERMS (Continue on reverse if necessary and identify by block number)  unconventional imaging, speckle imaging, phase retrieval, optical detection	
FIELD	GROUP	SUB-GROUP		
19. ABSTRACT (Continue on reverse if necessary and identify by block number)  This Final Report addresses key issues for development of a multiple aperture imaging system which could perform high resolution imaging at very long ranges for surveillance or discrimination. Multiple aperture systems can be used to realize extremely large optical apertures required for long-range, high-resolution systems. Our concept, which makes use of an array of intensity sensing subapertures (photon buckets), requires the simplest and potentially lowest cost hardware of any multiple aperture imaging system. The work described in this report is divided into three parts; a study of subaperture fill factors, a subaperture design, and a discussion of issues which relate to the performance of phase retrieval algorithms.				
20. DISTRIBUTION / AVAILABILITY OF ABSTRACT <input type="checkbox"/> UNCLASSIFIED/UNLIMITED <input checked="" type="checkbox"/> SAME AS RPT. <input type="checkbox"/> DTIC USERS			21. ABSTRACT SECURITY CLASSIFICATION UNCLASSIFIED	
22a. NAME OF RESPONSIBLE INDIVIDUAL P. D. HENSHAW			22b. TELEPHONE (Include Area Code) (617) 863-1060	22c. OFFICE SYMBOL

## TABLE OF CONTENTS

1	Introduction . . . . .	1
2	Effect of Subaperture Size to Spacing Ratio on Phase Retrieval Performance	3
2.1	Theoretical Analysis . . . . .	3
2.2	Computer Model of Aperture Area . . . . .	5
2.3	Simulation Results . . . . .	8
2.4	Dynamic Generation of Improved Support Constraints . . . . .	16
2.5	Conclusions . . . . .	16
3	Subaperture Design . . . . .	22
3.1	Derivation of Wavelength-Dependent Merit Functions . . . . .	22
3.2	Evaluation of Wavelength-Dependent Merit Functions . . . . .	24
3.2.1	Signal Shot Noise Limit . . . . .	24
3.2.2	Background Noise-limited Merit Function . . . . .	27
3.2.3	Detector Noise-limited Merit Function . . . . .	29
3.2.4	Subaperture Signal-to-Noise Ratio . . . . .	30
3.3	Subaperture Design . . . . .	35
3.3.1	Collection Optics . . . . .	36
3.3.2	Bandpass Filter . . . . .	38
3.3.3	Detector and Electronics . . . . .	38
3.3.4	Subaperture Parts List . . . . .	39
3.3.5	Mechanical Design . . . . .	40
3.3.6	Lasers . . . . .	42
3.4	Summary of Subaperture Design . . . . .	42
4	Key Issues for Phase Retrieval Algorithms . . . . .	43
4.1	Direct Phase Retrieval from Single Speckle Patterns . . . . .	43
4.2	Phase Retrieval Performance for Low SNR . . . . .	45
4.3	Target Parameter Influence on Phase Retrieval . . . . .	44
4.4	Investigation of the "Zero-lag" Problem . . . . .	45
4.5	Alternative Phase Retrieval Methods . . . . .	45
4.6	Subaperture Design . . . . .	46
5	Conclusions . . . . .	48
	References . . . . .	48

## LIST OF TABLES

1	Parameters for Signal-to-Noise Ratio Calculations . . . . .	31
2	Detector Parameters . . . . .	34
3	Aberration Blur (in milliradians) for a 50 mm Diameter Singlet Bent to Minimize Spherical Aberration. . . . .	37
4	Narrow Field-of-View Subaperture Parts List . . . . .	41
5	Summary of Key Issues for Phase Retrieval . . . . .	47

Approved For	
NTIS	✓
DTIC	
Unannounced	
Prescribed	
By	
Date	
Appr	
Just	
A-1	



## LIST OF FIGURES

1	Intensity distribution of sampled speckle with finite aperture area. . . . .	4
2	Algorithm for simulation of finite detector area. . . . .	7
3	Image expansion by four: initial $64 \times 64$ image (top left), image buffered to $256 \times 256$ (top right), propagated speckle pattern incident upon subaperture array (bottom left), and speckle image recorded by subaperture array (bottom right). . . . .	7
4	Histogram of ten speckle patterns for point sampled case. . . . .	8
5	Histograms of ten speckle images obtained by integrating incoherently over $4 \times 4$ (top) and $8 \times 8$ (bottom) pixel regions of the propagated image. . . . .	9
6	Histograms of ten speckle images obtained by integrating incoherently over $12 \times 12$ (top) and $16 \times 16$ (bottom) pixel regions of the propagated image. . . . .	10
7	IFTA performance with one thousand speckle patterns. . . . .	11
8	Images reconstructed with ten cycles of six hybrid input-output subcycles and four error reduction subcycles from one thousand speckle patterns with expansion by factor of four: control case (top left), integrating $1 \times 1$ (top right), $2 \times 2$ (middle left), $3 \times 3$ (middle right), and $4 \times 4$ (bottom left) squares, and target image (bottom right). . . . .	12
9	IFTA performance with one hundred speckle patterns. . . . .	13
10	Images reconstructed with ten cycles of six hybrid input-output subcycles and four error reduction subcycles from one hundred speckle patterns with expansion by factor of four: control case (top left), integrating $1 \times 1$ (top right), $2 \times 2$ (middle left), $3 \times 3$ (middle right), and $4 \times 4$ (bottom left) squares, and target image (bottom right). . . . .	14
11	Images reconstructed with ten cycles of fifteen hybrid input-output subcycles and ten error reduction subcycles from one hundred speckle patterns with expansion by factor of four: control case (top left), integrating $1 \times 1$ (top right), $2 \times 2$ (middle left), $3 \times 3$ (middle right), and $4 \times 4$ (bottom left) squares, and target image (bottom right). . . . .	15
12	IFTA performance with one hundred speckle patterns with standard (square) and ideal support constraints. . . . .	17
13	IFTA performance with one hundred speckle patterns and alternate support constraints obtained from autocorrelation estimate. . . . .	18
14	Images reconstructed with ten cycles of six hybrid input-output subcy-	

	cles and four error reduction subcycles and autocorrelation mask support from one hundred speckle patterns with expansion by factor of sixteen: control case (top left), point sampled case (top right), and integrating $4 \times 4$ (middle left), $8 \times 8$ (middle right), $12 \times 12$ (bottom left), and $16 \times 16$ (bottom right) squares of pixels in propagated image. . . .	19
15	Images reconstructed with ten cycles of six hybrid input-output subcycles and four error reduction subcycles and support constraint from optimal (least area) intersection of two offset autocorrelation masks from one hundred speckle patterns with expansion by factor of sixteen: control case (top left), point sampled case (top right), and integrating $4 \times 4$ (middle left), $8 \times 8$ (middle right), $12 \times 12$ (bottom left), and $16 \times 16$ (bottom right) squares of pixels in propagated image. . . . .	20
16	Atmospheric transmission versus wavelength. . . . .	25
17	Quantum efficiency versus wavelength for various detectors. . . .	26
18	Signal-limited merit function versus wavelength. . . . .	27
19	Sky radiance versus angle between the sun and look directions for Nd:YAG and frequency-doubled Nd:YAG. . . . .	28
20	Sky spectral radiance versus wavelength. . . . .	29
21	Background limited merit function versus wavelength. . . . .	30
22	Detection limited merit function versus wavelength. . . . .	31
23	Number of signal photons versus range. . . . .	32
24	Comparison of existing and ideal detector at short and long wavelengths.	33
25	Comparison of signal-to-noise ratio using off-the-shelf detectors. .	34
26	Comparison of signal-to-noise ratio using improved detectors. . . .	35
27	Schematic diagram of a subaperture. . . . .	36
28	Central wavelength versus angle of incidence for a Nd:glass laser band-pass filter. . . . .	39
29	Flow chart for image reconstruction from sampled speckle pattern intensities. . . . .	44

### **Abstract**

This Final Report addresses key issues for development of a multiple aperture imaging system which could perform high resolution imaging at very long ranges for surveillance or discrimination. Multiple aperture systems can be used to realize extremely large optical apertures required for long-range, high-resolution systems. Our concept, which makes use of an array of intensity sensing subapertures (photon buckets), requires the simplest and potentially lowest cost hardware of any multiple aperture imaging system. The work described in this report is divided into three parts; a study of subaperture fill factors, a subaperture design, and a discussion of issues which relate to the performance of phase retrieval algorithms.

## 1 Introduction

This Final Report summarizes work on contract N00014-90-C-0199, Optical Subaperture Development, performed for the Office of Naval Research during the period 1 September, 1990 to 1 April 1991.

This work addresses key issues for development of a multiple aperture imaging system which could perform high resolution imaging at very long ranges for surveillance or discrimination. Multiple aperture systems can be used to realize extremely large optical apertures required for long-range, high-resolution systems. Our concept, which makes use of an array of intensity sensing subapertures (photon buckets), requires the simplest and potentially lowest cost hardware of any multiple aperture imaging system. Therefore, there is a large payoff for demonstrating the feasibility of this concept. Key issues for this imaging technique fall into three areas:

1. Can a photon-counting subaperture be built for a reasonable cost so that a large array is affordable?
2. Can an array of subapertures collect the information required to form an image?
3. Is the algorithm used to perform phase retrieval from the intensity measurements suitably robust given the quality of detected speckle intensity data?

The work described in this report is divided into three parts: a study of subaperture fill factors, which addresses issue 2, a subaperture design, which addresses issue 1 and 2, and a discussion of issues which relate to the performance of phase retrieval algorithms, which details our approach to issue 3.

The first section discusses the effect of the subaperture collecting area on system performance. Previous work assumed point sampling of the speckle pattern, and ignored the effect of low pass filtering on the autocorrelation estimate due to the finite area of real subapertures.[1-3] We have modified our multiple aperture system to include the effects of finite area subapertures. The theoretical and simulated speckle statistics have been compared to verify the simulation correctness. Reconstruction of image from speckle patterns sampled with different array fill factors has been performed. We show that acceptable image reconstructions can be achieved with relatively high array fill factors. This result is significant since it indicates a large fraction of the laser light falling on a subapertures array may be utilized for image reconstruction.

The second section discusses subaperture design considerations which are valid for any ground-based multiple aperture system. Three figures of merit are presented; these figures of merit point to the general conclusion that operation at



longer wavelengths in the near IR, where quantum-limited detection is possible, provides the best system performance.

In the third section, we present a short discussion of the key issues for our multiple aperture system associated with the use of phase retrieval and the most likely solutions for each of these issues.

Future work should clearly be oriented toward the key issues associated with our multiple aperture imaging concept. As discussed in the third section, construction of a cost-effective subaperture with the required sensitivity and low-noise performance is not an issue. Background suppression to a level sufficient to observe laser illuminated targets during clear daytime conditions can clearly be achieved. The array requirements can also be met. The alignment tolerance required by the subaperture design presented in Section 3 is well within the capabilities and fabrication techniques. As discussed in Section 2, the array can be built with a linear fill factor of greater than 50% providing sufficient photon collection capability for a real system. The key issues as currently perceived all center on the performance of the phase retrieval algorithm. If phase retrieval works for a wide variety of targets and noise conditions, then simple detector systems which measure only intensity can be used. These detector systems are clearly cheaper than more complicated detectors which must measure phase or the time history of a received waveform.

## 2 Effect of Subaperture Size to Spacing Ratio on Phase Retrieval Performance

In SPARTA's previous analysis of image reconstruction by iterative phase retrieval, speckle patterns were simulated at a single discrete point for each detector element. This simulation technique is equivalent to sampling speckle patterns with point ("zero area") detectors — which, in a real system, would obviously lead to the collection of very small numbers of photons. In support of the design of prototype subaperture assemblies, therefore, SPARTA examined the impact of aperture size on the performance of unconventional imaging systems.

### 2.1 Theoretical Analysis

The collecting area of a subaperture can be approximated as a point if it is small enough so that the incident electromagnetic field is approximately constant over the subaperture area. As the collecting area becomes larger, the field incident on opposite sides of the subaperture becomes partially decorrelated, introducing additional degrees of freedom into the measured sample. For large signal levels (negligible shot noise), the statistical distribution of the measured intensities is given by a  $\chi^2$  distribution [4] which is characterized by the probability density function [5]

$$p\left(\frac{I}{\bar{I}}\right) = \frac{\mathcal{M}}{\Gamma(\mathcal{M})} \left(\frac{\mathcal{M}I}{\bar{I}}\right)^{\mathcal{M}-1} \exp\left(\frac{-\mathcal{M}I}{\bar{I}}\right) \quad (1)$$

where

$p$  is the probability density function,

$I$  is the measured intensity,

$\bar{I}$  is the expected (mean) intensity, and

$\mathcal{M}$  is the number of degrees of freedom in each (real and imaginary) component of the field collected by each subaperture.

Subaperture designs which integrate the incident speckle coherently cannot introduce additional degrees of freedom in the speckle statistics; for these systems,

$$\mathcal{M} = 1 \quad (2)$$

and equation (1) reduces to the classical negative exponential distribution

$$p\left(\frac{I}{\bar{I}}\right) = \exp\left(\frac{-I}{\bar{I}}\right). \quad (3)$$

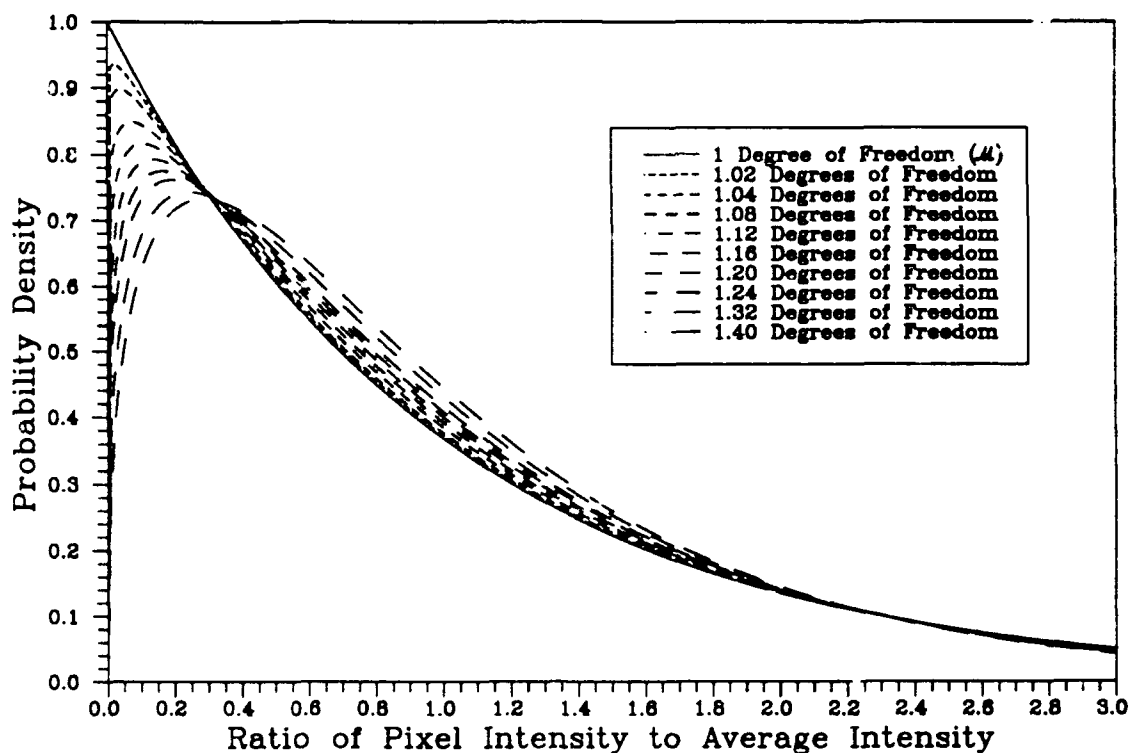


Figure 1. Intensity distribution of sampled speckle with finite aperture area.

Subaperture designs which integrate the incident speckle incoherently, on the other hand, do introduce additional degrees of freedom, and equation (1) yields the family of distributions illustrated in Figure 1.

The number of degrees of freedom introduced by a subaperture design which integrates incoherently is given, in general, by the formula [6]

$$\mathcal{M} = \frac{A^2}{\int_{-\infty}^{\infty} \int_{-\infty}^{\infty} R_S(\Delta x, \Delta y) |\mu(\Delta x, \Delta y)|^2 d\Delta x d\Delta y} \quad (4)$$

where

$A$  is the area of the subaperture,

$R_S(\Delta x, \Delta y)$  is the optical transfer function of the subaperture, and

$\mu(\Delta x, \Delta y)$  is the complex coherence factor of the incident speckle.

For a square subaperture and Gaussian speckle correlation,

$$R_S(\Delta x, \Delta y) = A \Lambda\left(\frac{2\Delta x}{s}\right) \Lambda\left(\frac{2\Delta y}{s}\right) \quad (5)a$$

$$\mu(\Delta x, \Delta y) = \exp \left( \frac{-\pi (\Delta x^2 + \Delta y^2)}{2S} \right) \quad (5b)$$

where

$\Lambda(x)$  is the triangle function defined by the relationship  $\Lambda(x) = \max(1 - |x|, 0)$ ,

$s$  is the length of each side of the subaperture, and

$S$  is the speckle coherence area.

The speckle coherence area is defined by the relationship

$$S = \int_{-\infty}^{\infty} \int_{-\infty}^{\infty} |\mu(\Delta x, \Delta y)|^2 d\Delta x d\Delta y. \quad (6)$$

Combining equations (4), (5a), and (5b) and evaluating the integrals,

$$\mathcal{M} = \left( \frac{1}{\sqrt{\frac{S}{A}} \operatorname{erf} \left( \sqrt{\frac{\pi A}{S}} \right) - \frac{S}{\pi A} \left( 1 - \exp \left( \frac{-\pi A}{S} \right) \right)} \right)^2 \quad (7)$$

For a subaperture that is small compared to the speckle size ( $A \ll S$ ),

$$\mathcal{M} \approx 1 + \frac{A}{S} \quad (8)$$

This approximation provides a rule of thumb for quick estimation of the number of degrees of freedom in each component for the cases of interest.

## 2.2 Computer Model of Aperture Area

SPARTA developed a computer model of the effects of subaperture collecting area, which is illustrated in Figure 2. The new model adds a border of background pixels to the initial speckled image of the target before the image is propagated to the aperture plane. The propagation algorithm is equivalent to a Fourier transform in that the resolution (pixel size) of the aperture plane image is inversely proportional to the initial frame size. The border around the initial image thus produces a proportionally higher resolution at the aperture plane. The

pixels falling on each subaperture are then summed either coherently or incoherently depending upon the subaperture design, corresponding to integration of the incident field or intensity over the collecting area of the subaperture.

The aperture model was integrated into SPARTA's speckle simulation program (SPECKSIM). Initially, speckle patterns were simulated with image expansion by four (from a  $64 \times 64$  initial image to a  $256 \times 256$  speckle pattern) and integrated incoherently over  $1 \times 1$ ,  $2 \times 2$ ,  $3 \times 3$ , and  $4 \times 4$  squares of pixels in the propagated speckle patterns with subaperture spacing (center to center) of four pixels in each dimension, as illustrated in Figure 3. Speckle patterns for a control case were generated without expanding the image, providing a meaningful comparison with previous results. The reconstruction results obtained with these cases, described below, provided evidence that the model was working as expected but a doubt remained as to the correct interpretation of the results. The case of "integration" over a  $1 \times 1$  square is in fact point sampled, just like the control case (speckle patterns generated without expanding the image). The case of integration over a  $2 \times 2$  square, on the other hand, is actually a sum of four point samples representing the corners of a  $1 \times 1$  square; these samples are necessarily have more degrees of freedom than the true average over a  $1 \times 1$  square (area fill factor of 6.25%), but may not have as many degrees of freedom as the true average over a  $2 \times 2$  square (area fill factor of 25%). The exact size of the aperture that was represented was not determined.

The uncertainty in the equivalent subaperture area was reduced to an acceptable level by simulating speckle patterns with image expansion by sixteen (from a  $64 \times 64$  initial image to a  $1024 \times 1024$  speckle pattern) and integration over regions of  $1 \times 1$  (point sampled),  $4 \times 4$ ,  $8 \times 8$ ,  $12 \times 12$ , and  $16 \times 16$  pixels of the propagated speckle pattern.

Normalized histograms of the intensity values of sets of ten simulated speckle patterns were compared to the distributions predicted by equation (1) to validate the model. The cases integrated coherently and the point sampled cases (including the control case), for which  $\mathcal{M} = 1$ , all conformed to the negative exponential distribution predicted by equation (1). Figure 4 shows a representative histogram from these cases.

The histograms for the cases integrated incoherently over multiple pixels exhibited a tendency to cluster near the distribution maximum, as illustrated in Figure 5 and Figure 6. The middle of the three dashed curves in each plot indicates the approximate theoretical distribution obtained from equation (4). The targets in the initial image spanned nearly half of each dimension of the image frame, so speckle patterns were simulated using a smaller target area to determine whether the target area was a contributing factor. The speckle patterns generated from the smaller

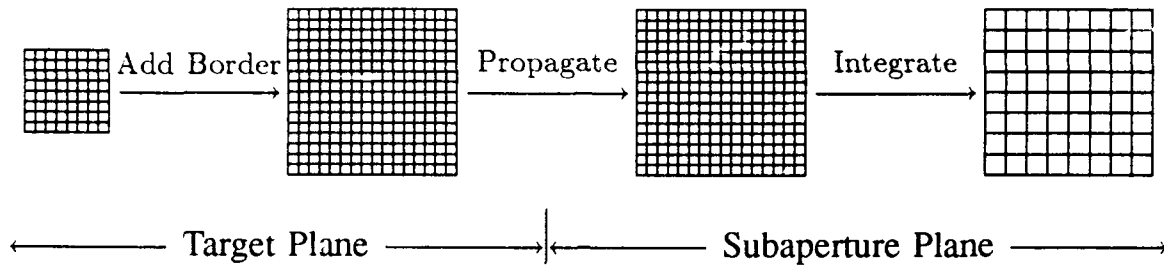


*Figure 2. Algorithm for simulation of finite detector area.*



*Figure 3. Image expansion by four: initial  $64 \times 64$  image (top left), image buffered to  $256 \times 256$  (top right), propagated speckle pattern incident upon subaperture array (bottom left), and speckle image recorded by subaperture array (bottom right).*

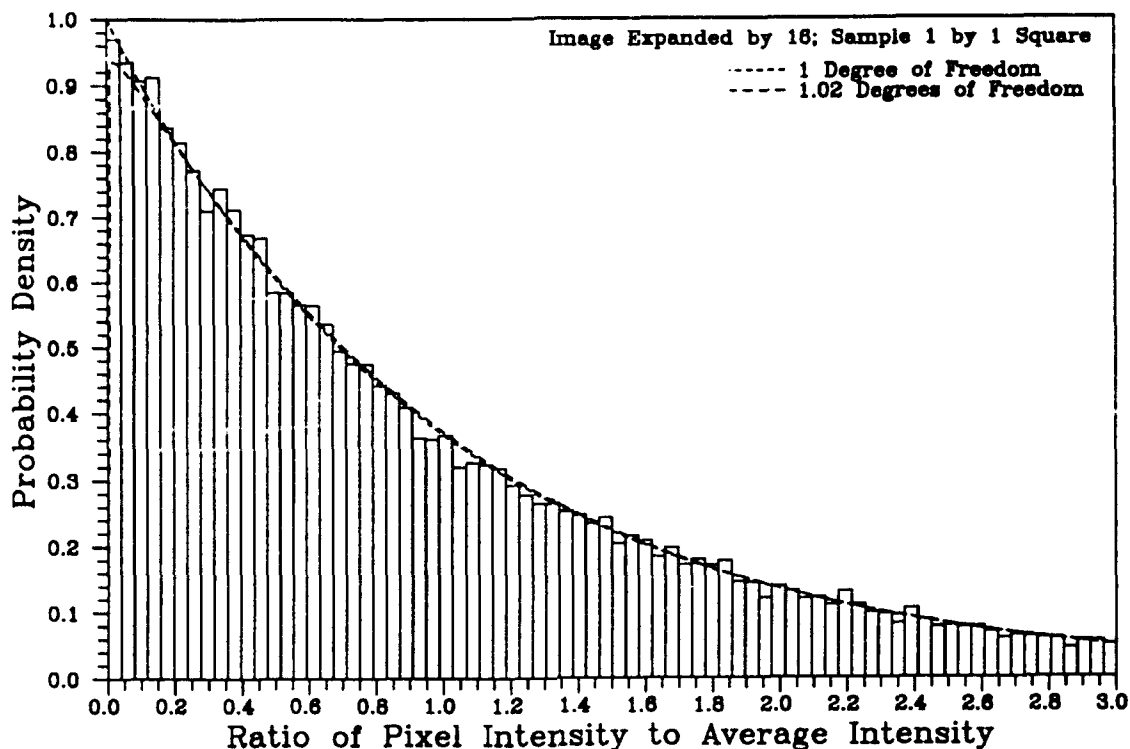


Figure 4. Histogram of ten speckle patterns for point sampled case.

target exhibited similar behavior, though not as severely.

The speckle statistics illustrated here are all generated using the same set of pseudorandom numbers, but speckle samples generated with a different randomization were examined and found to exhibit similar behavior. Differences in the propagated speckle patterns are not apparent under rigorous visual examination of printed images.

### 2.3 Simulation Results

The iterative Fourier transform algorithm (IFTA) was executed using autocorrelation estimates obtained from speckle patterns corresponding to various subaperture fill factors simulated as described above. The subaperture collecting areas were assumed to be square and the signal was assumed to be sufficiently strong so that noise was not significant. Unless otherwise noted, images were reconstructed using ten phase retrieval cycles of six hybrid input/output (HIO) subcycles and four error reduction subcycles and a square support constraint of one fourth of the image area centered in the image frame.

Images were initially recovered using autocorrelation estimates obtained from one thousand speckle patterns propagated with an image expansion factor of four and sample areas of  $1 \times 1$ ,  $2 \times 2$ ,  $3 \times 3$ , and  $4 \times 4$  pixels with subaperture grid spacing

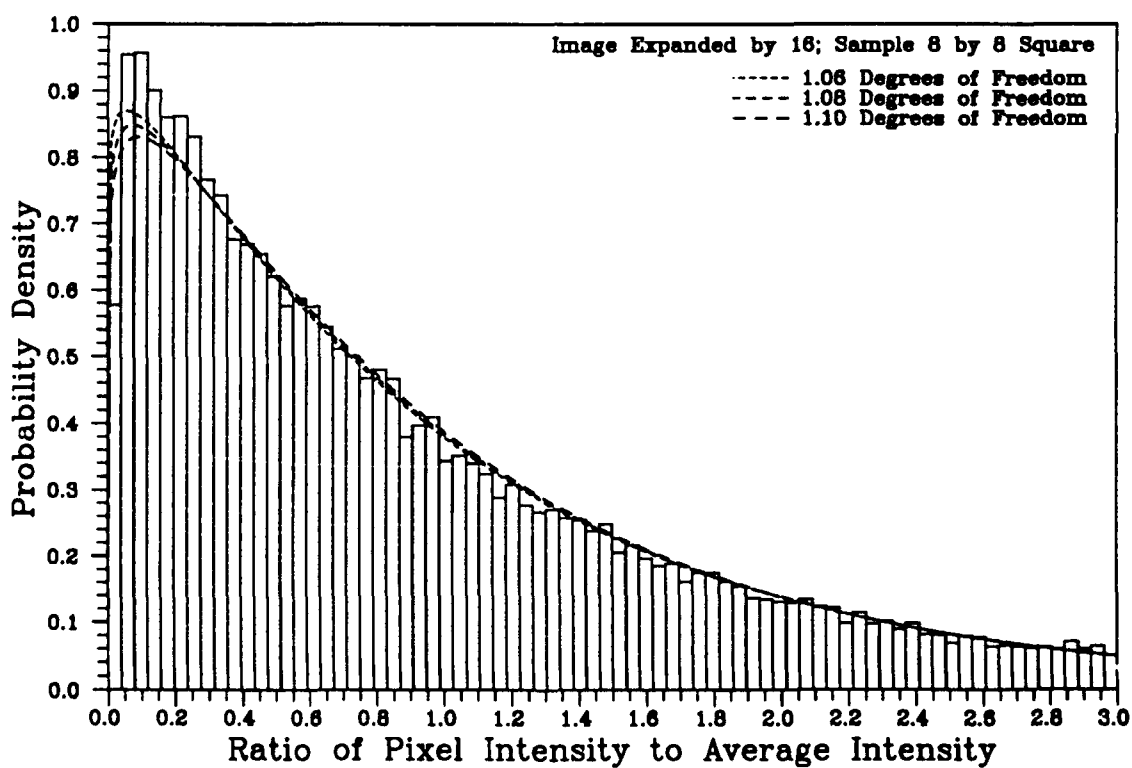
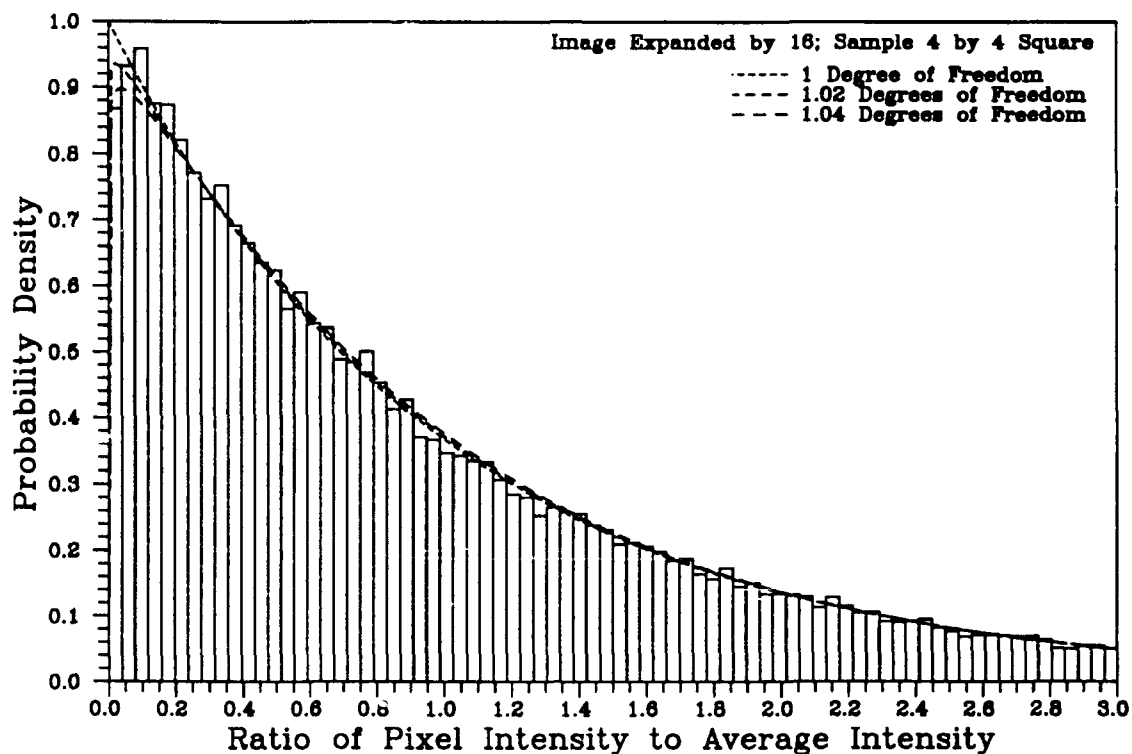


Figure 5. Histograms of ten speckle images obtained by integrating incoherently over  $4 \times 4$  (top) and  $8 \times 8$  (bottom) pixel regions of the propagated image.



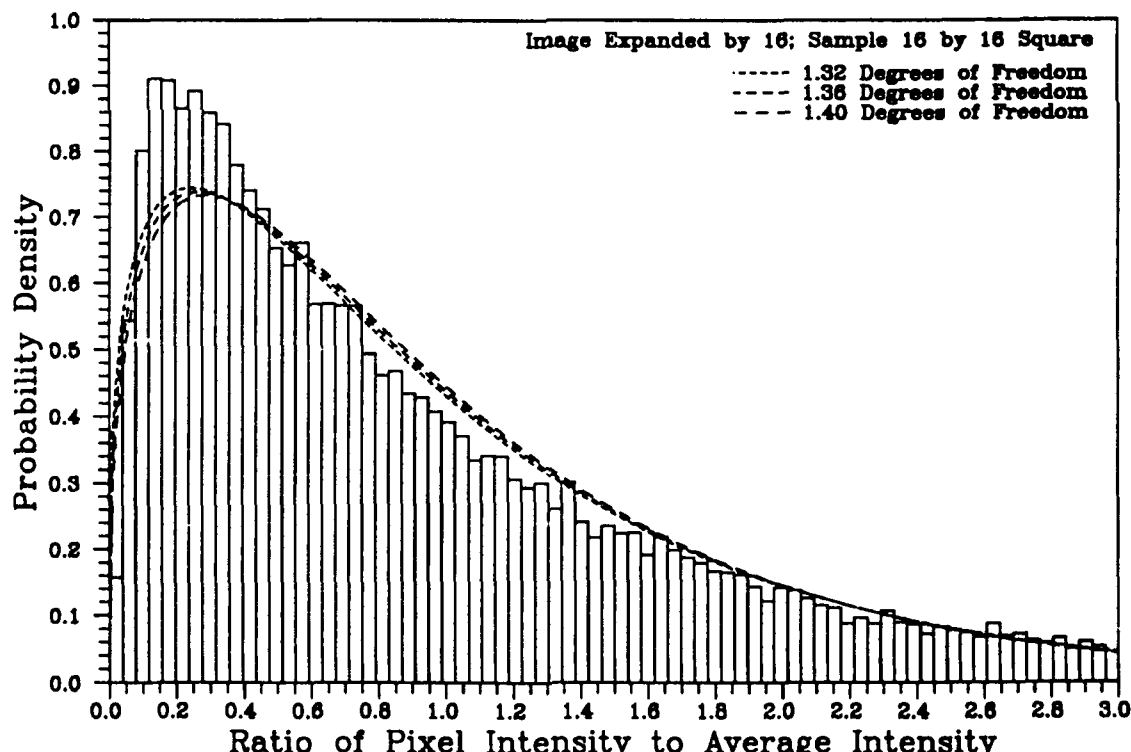
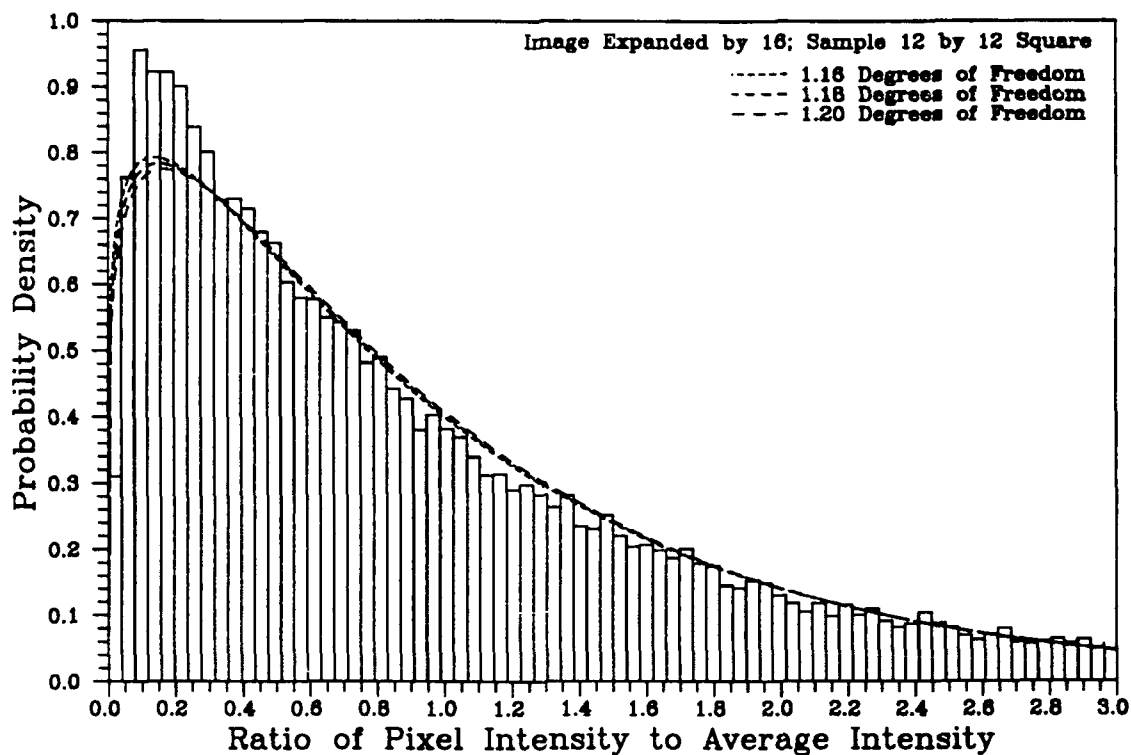


Figure 6. Histograms of ten speckle images obtained by integrating incoherently over  $12 \times 12$  (top) and  $16 \times 16$  (bottom) pixel regions of the propagated image.

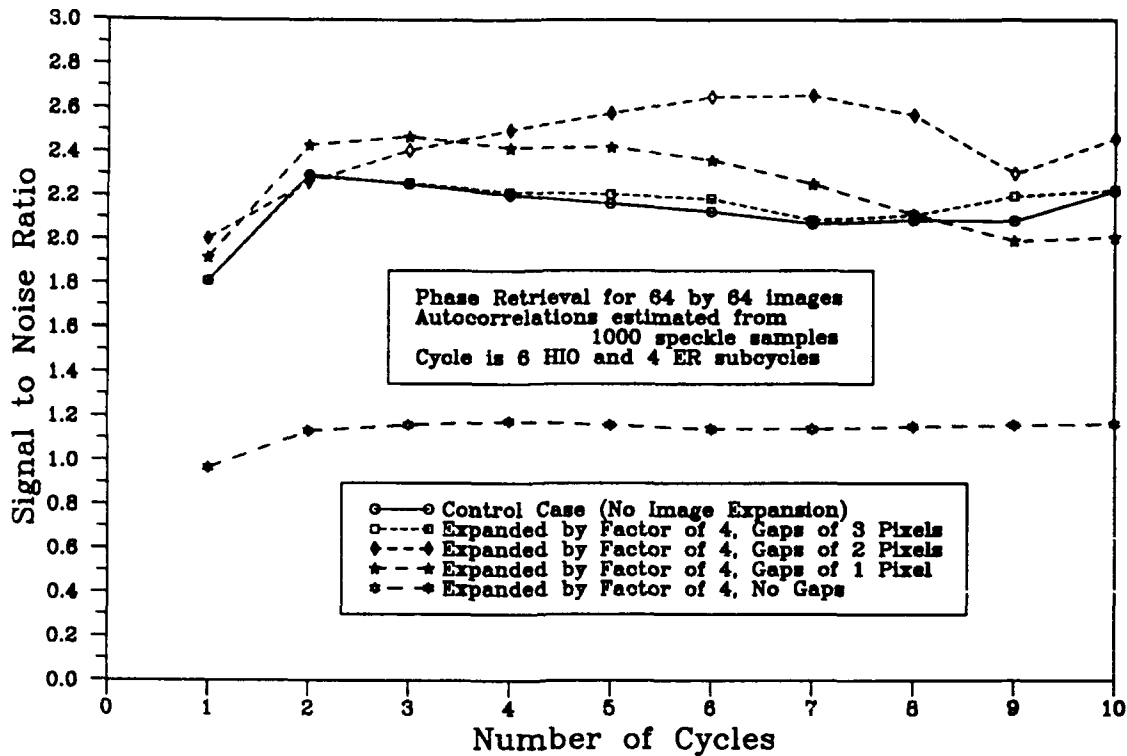
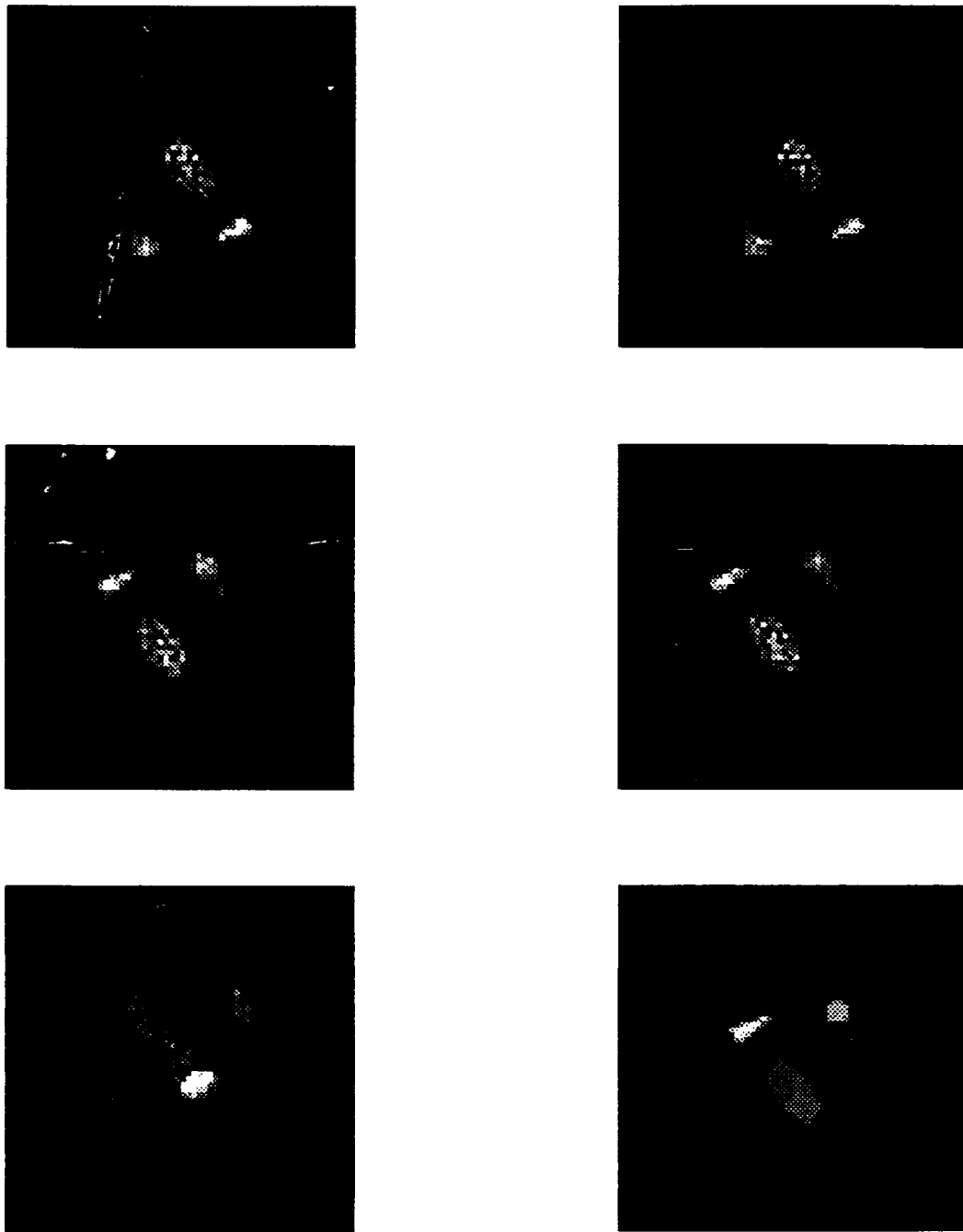


Figure 7. IFTA performance with one thousand speckle patterns.

(center to center) of four pixels in each dimension. The IFTA reconstruction succeeded for all except the  $4 \times 4$  case with no evidence of gradual degradation as shown in Figure 7; this was the first indication of binary performance (success or failure) of image reconstruction that was observed in all subsequent attempts. Figure 8 shows the final reconstructed images.

Images were also recovered using autocorrelation estimates obtained from one hundred speckle samples using the same four integration areas. The performance was generally similar to the results obtained with one thousand speckle patterns, except that the case  $3 \times 3$  sample area joined the case of  $4 \times 4$  sample area in failing to reconstruct. A second attempt at reconstruction using fifteen HIO and ten ER subcycles produced similar results; both are shown in Figure 9. Reconstructed images for these cases are shown in Figure 10 and Figure 11.

Images of  $64 \times 64$  pixels were expanded by a factor of sixteen (to  $1024 \times 1024$  pixels) before propagation, both to further investigate the binary behavior of the reconstruction algorithm and to reduce the ambiguity in the sampled area to an acceptable level. Cases were sampled by integrating  $1 \times 1$  (point sampling),  $4 \times 4$ ,  $8 \times 8$ ,  $12 \times 12$ , and  $16 \times 16$  subareas of the  $16 \times 16$  square corresponding to each subaperture, and a control case was propagated without expansion as in the previous simulations. The initial reconstructions with the square support constraint failed for all except the point sampled case and the control case, which was truly surprising



*Figure 8. Images reconstructed with ten cycles of six hybrid input-output subcycles and four error reduction subcycles from one thousand speckle patterns with expansion by factor of four: control case (top left), integrating  $1 \times 1$  (top right),  $2 \times 2$  (middle left),  $3 \times 3$  (middle right), and  $4 \times 4$  (bottom left) squares, and target image (bottom right).*

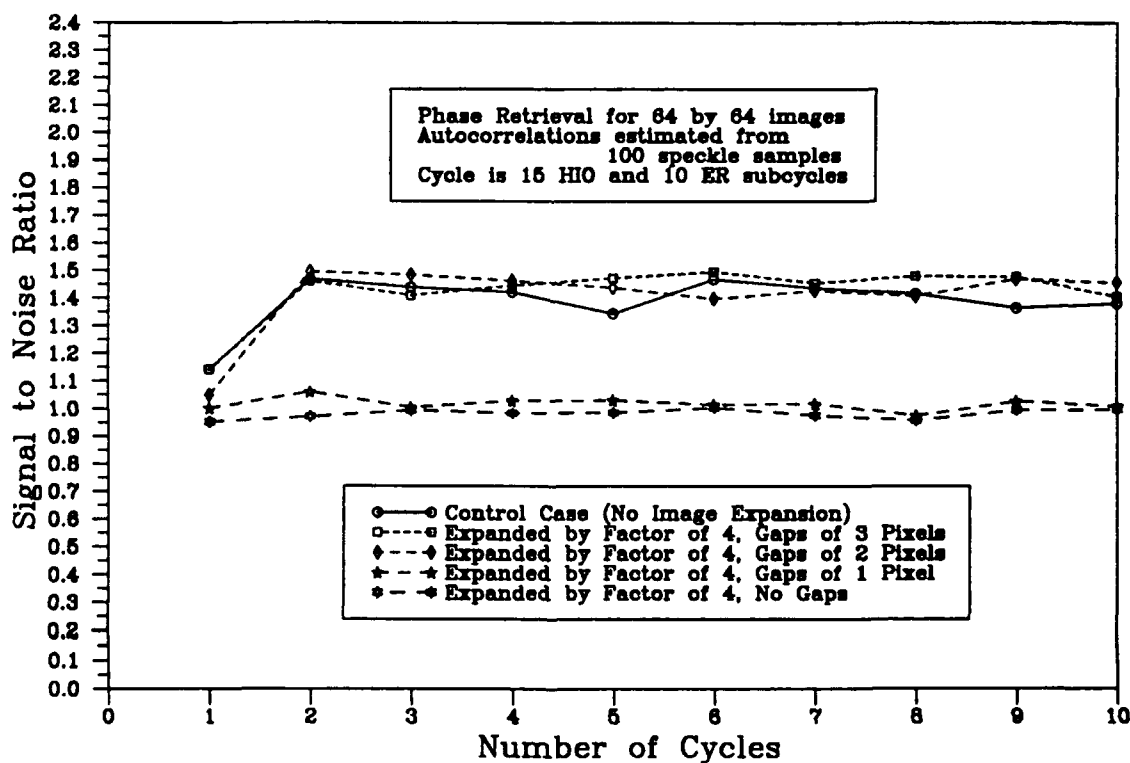
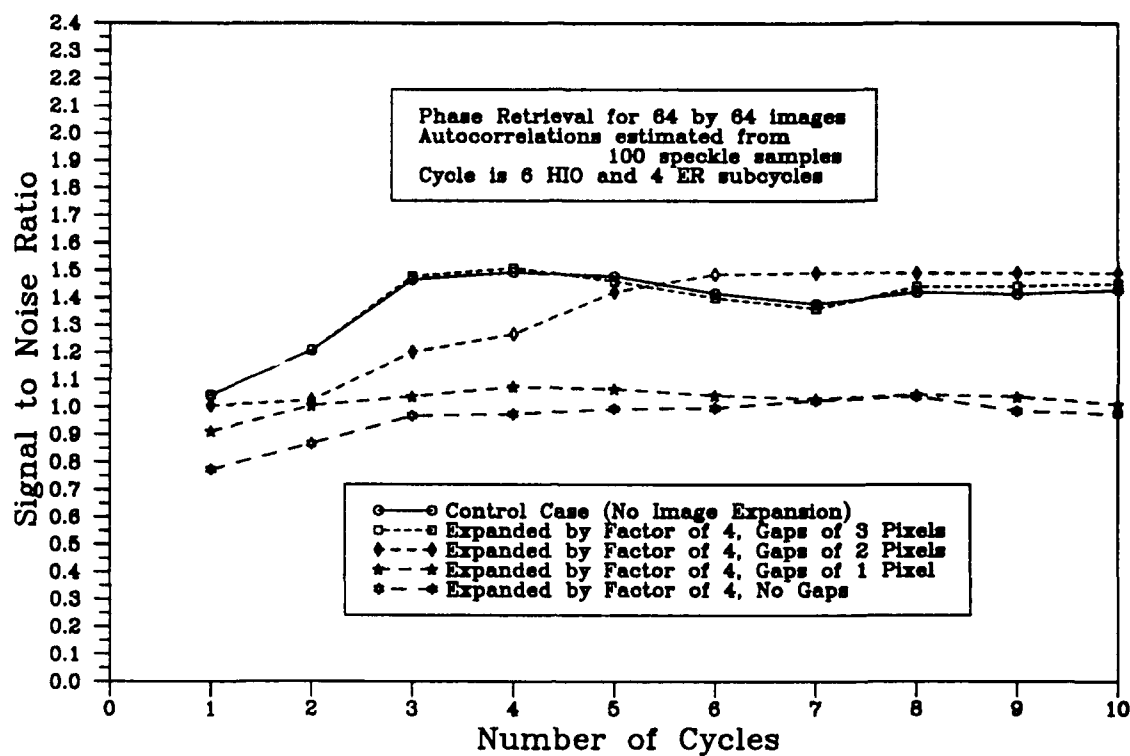
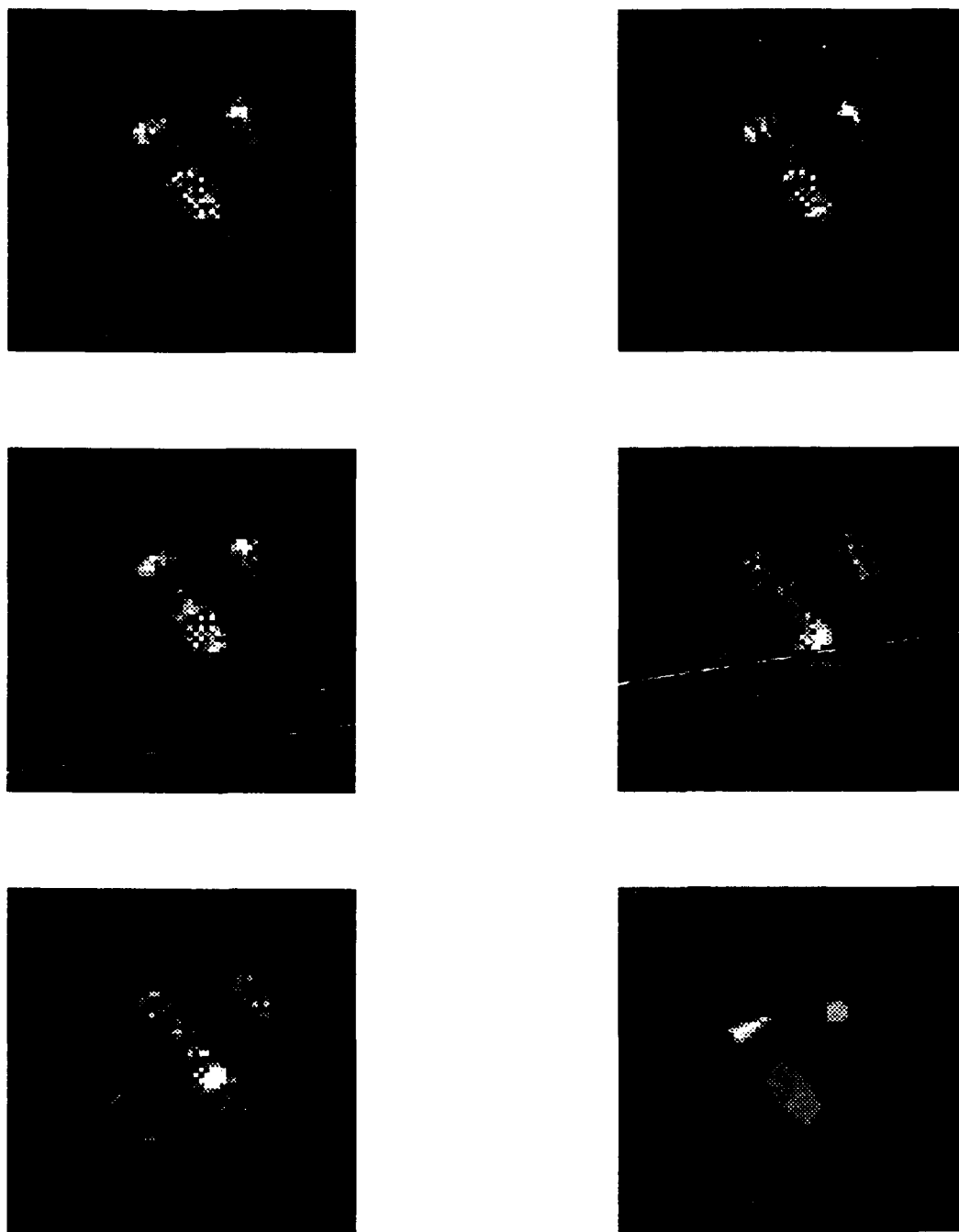
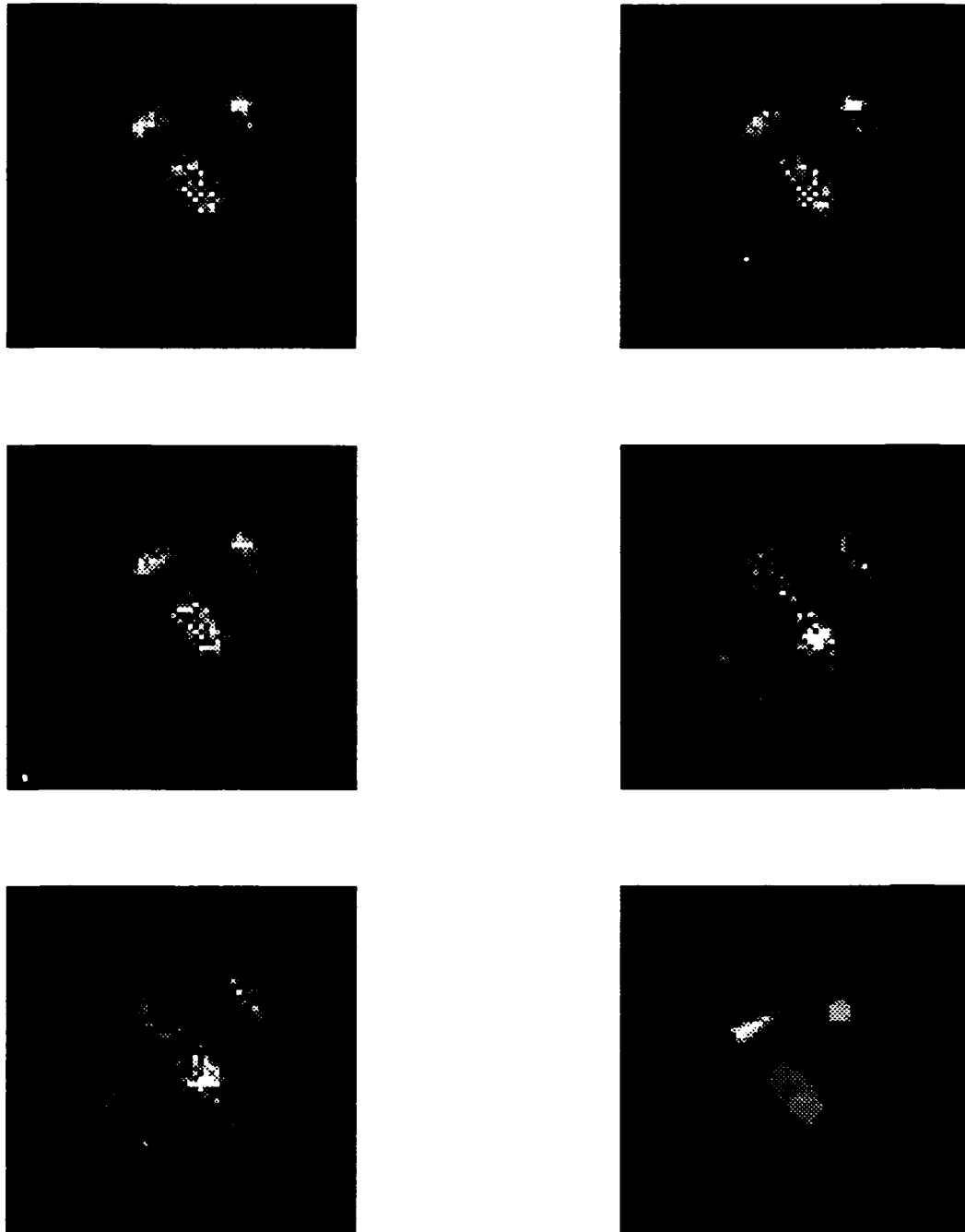


Figure 9. IFTA performance with one hundred speckle patterns.



*Figure 10. Images reconstructed with ten cycles of six hybrid input-output subcycles and four error reduction subcycles from one hundred speckle patterns with expansion by factor of four: control case (top left), integrating  $1 \times 1$  (top right),  $2 \times 2$  (middle left),  $3 \times 3$  (middle right), and  $4 \times 4$  (bottom left) squares, and target image (bottom right).*



*Figure 11. Images reconstructed with ten cycles of fifteen hybrid input-output subcycles and ten error reduction subcycles from one hundred speckle patterns with expansion by factor of four: control case (top left), integrating  $1 \times 1$  (top right),  $2 \times 2$  (middle left),  $3 \times 3$  (middle right), and  $4 \times 4$  (bottom left) squares, and target image (bottom right).*

in the light of the results obtained with the image expanded by four. Images were successfully reconstructed for all cases using the ideal support constraint obtained by making a binary mask from the target image, with which all cases reconstructed. These results are shown in Figure 12.

#### 2.4 Dynamic Generation of Improved Support Constraints

The ideal support constraint virtually guarantees the success of the phase retrieval process, but there is no known technique to reliably obtain it in an operational system. The binary mask of the autocorrelation can be obtained easily, and yielded satisfactory results in the phase retrieval operation with only one case (the  $16 \times 16$  integration area) failing to reconstruct, as shown in Figure 13. A smaller than standard error window was necessary to characterize the performance of this constraint because the images reconstructed significantly off center due to the large size of the mask. The reconstructed images are shown in Figure 14.

The autocorrelation mask is far from the optimal support constraint that can be obtained in an operational system. Fienup [7] describes a process for obtaining a constraint intersecting three offset copies of this mask, but his approach is dependent upon concavities in the autocorrelation which may or may not exist. Nevertheless, two offset copies of the autocorrelation threshold can always be intersected to obtain a support constraint, provided that the center of one copy lies within the bounds of the other. Many possible overlaps exist, so a rule for choosing the optimal overlap is necessary; the overlap of minimum intersection area was used in this brief investigation to produce the smallest obtainable support. The performance obtained with this optimized support is also shown in Figure 13, and the reconstructed images are shown in Figure 15.

#### 2.5 Conclusions

Images were successfully reconstructed from simulated speckle patterns recorded by square subapertures and area fill factors exceeding fifty percent. This result means that unconventional imaging systems can be built with reasonably large ratios of subaperture spacing (the fill factor). Fill factors approaching one permit the construction of highly photon-efficient systems, thus reducing the laser illuminator requirements.

Image reconstruction using the standard IFTA exhibited highly binary (success or failure) performance for all cases examined; no gradual degradation was observed. This result means that the subaperture design for an operational system absolutely must allow some margin between the subaperture size and the performance cliff if the system is to be robust. Area fill factors of fifty percent appear to be acceptable, but further investigation is required to determine how much higher

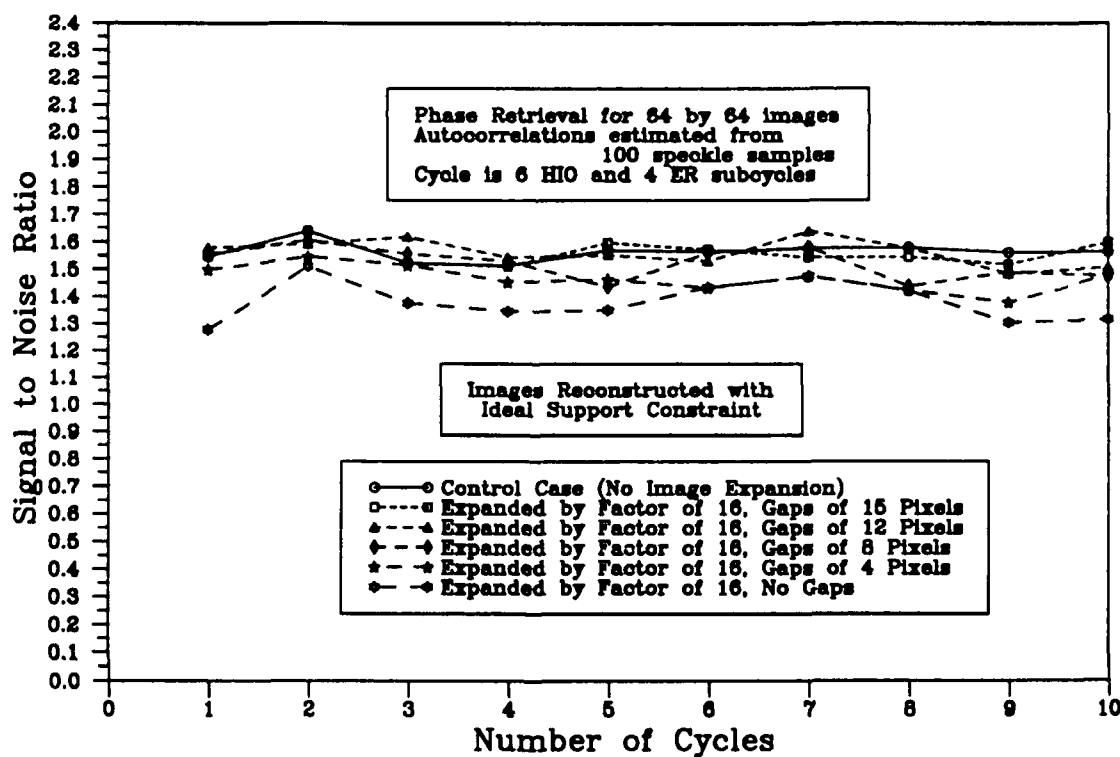
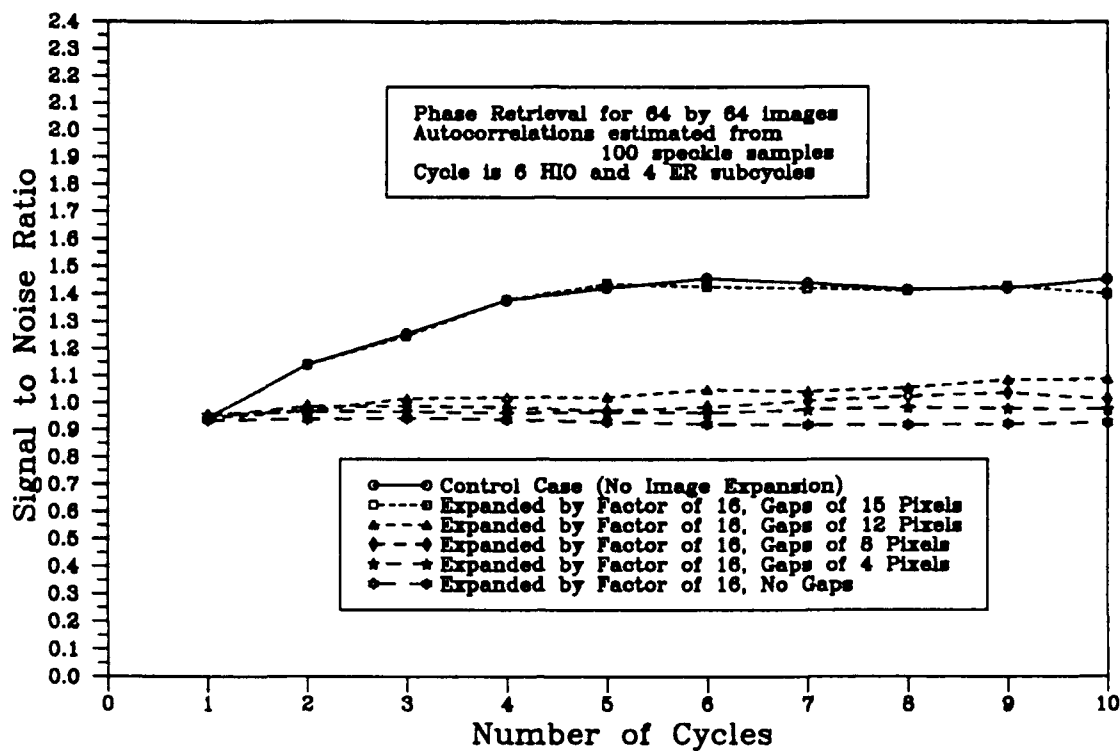


Figure 12. IFTA performance with one hundred speckle patterns with standard (square) and ideal support constraints.



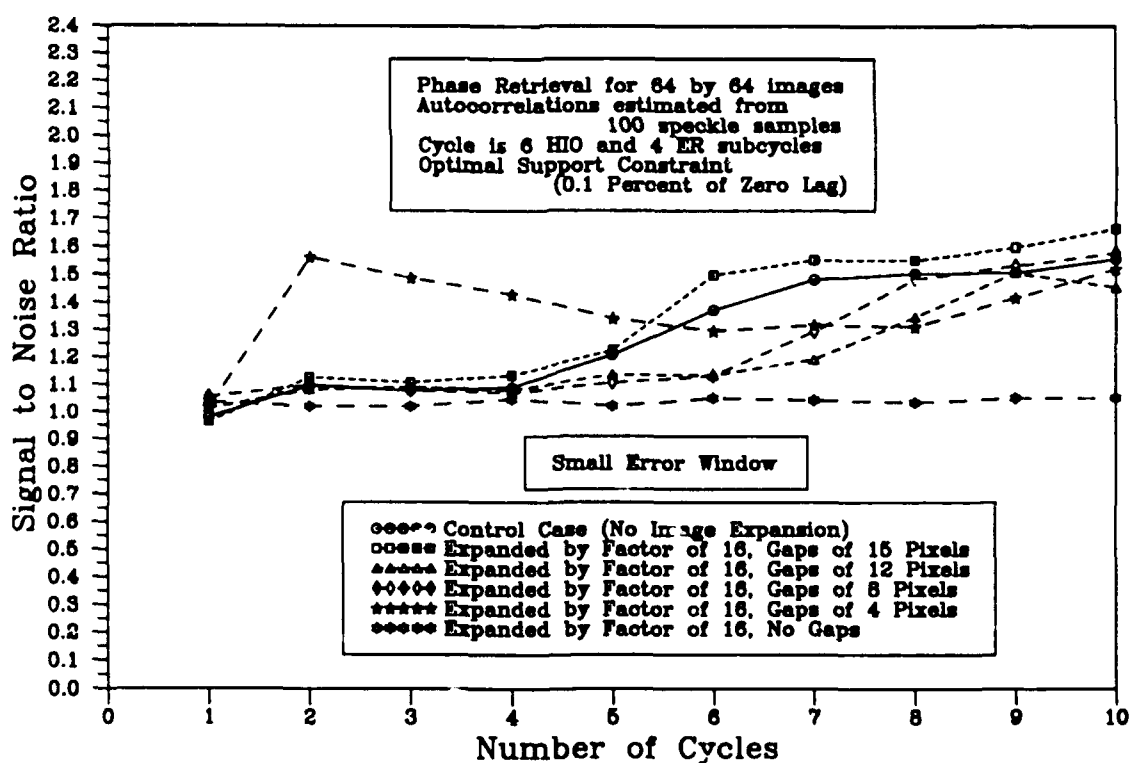
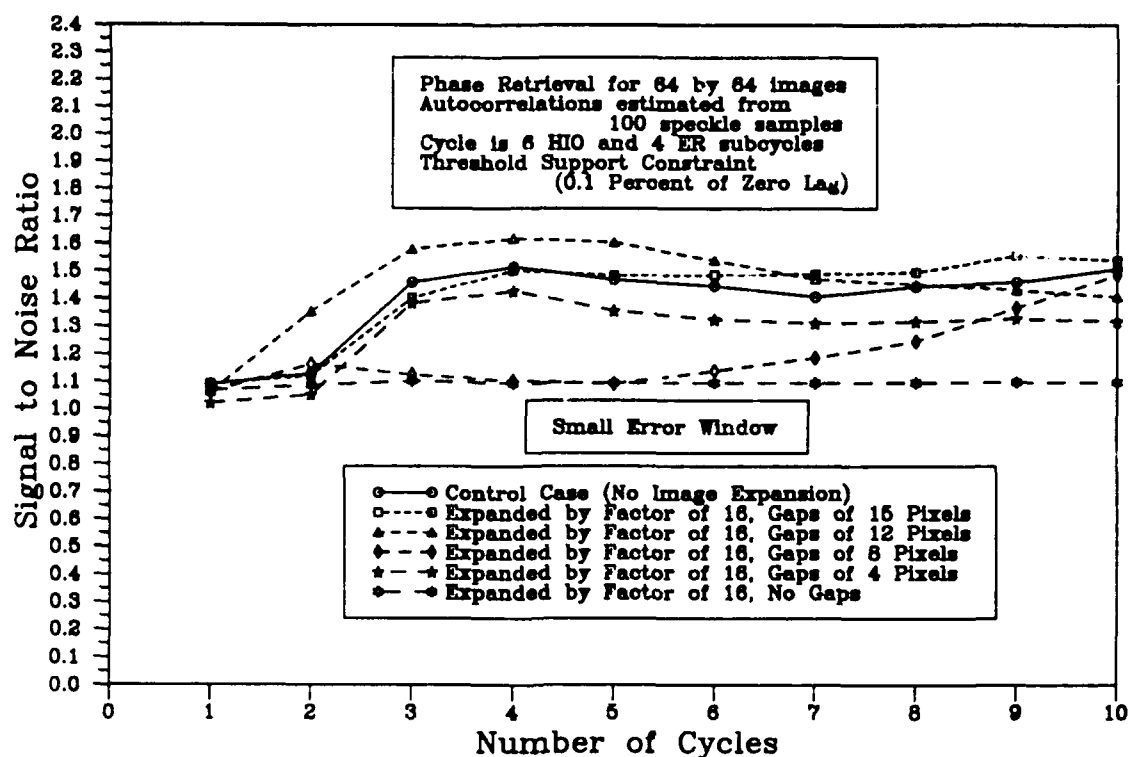
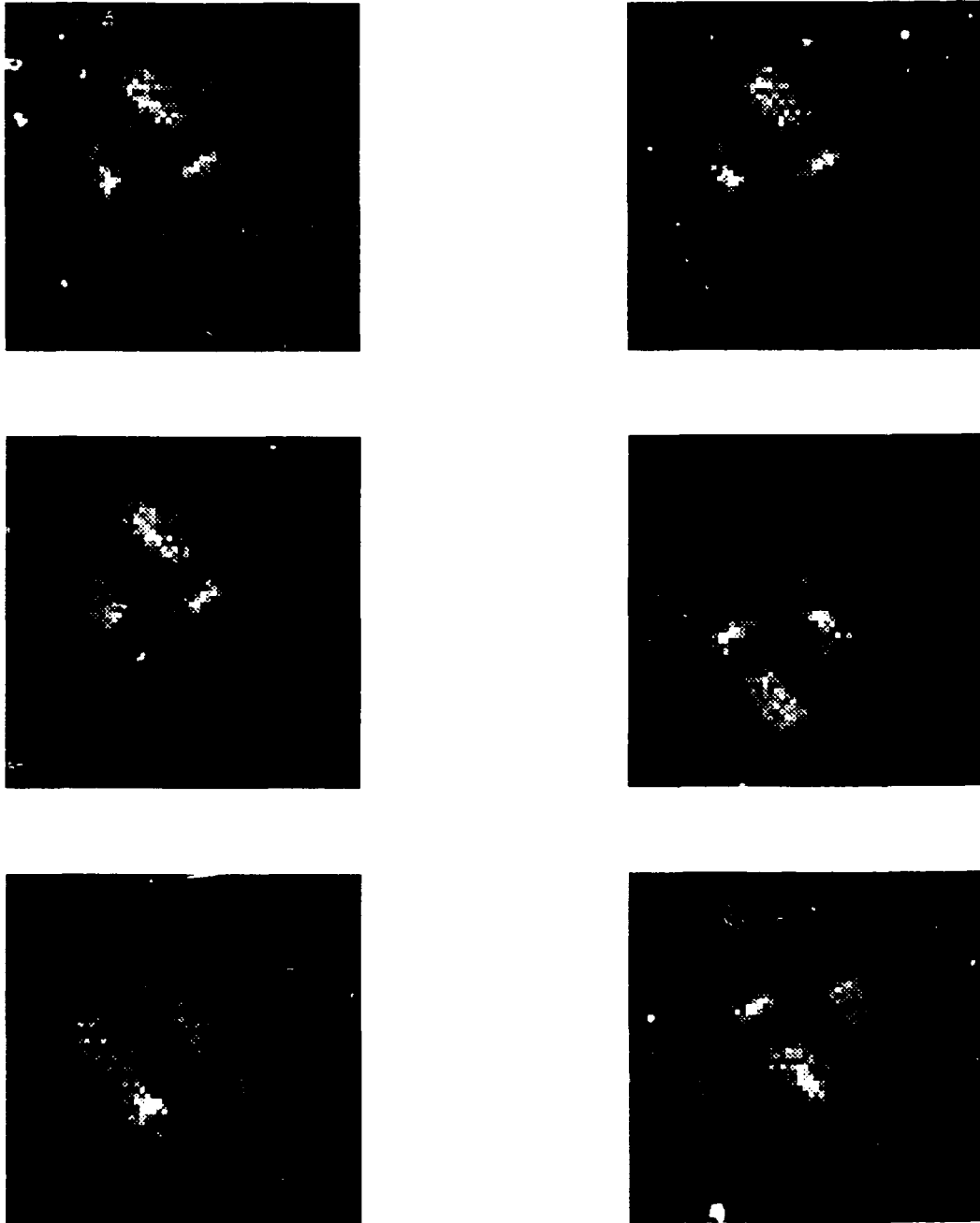


Figure 13. IFTA performance with one hundred speckle patterns and alternate support constraints obtained from autocorrelation estimate.



*Figure 14. Images reconstructed with ten cycles of six hybrid input-output subcycles and four error reduction subcycles and autocorrelation mask support from one hundred speckle patterns with expansion by factor of sixteen: control case (top left), point sampled case (top right), and integrating  $4 \times 4$  (middle left),  $8 \times 8$  (middle right),  $12 \times 12$  (bottom left), and  $16 \times 16$  (bottom right) squares of pixels in propagated image.*



*Figure 15. Images reconstructed with ten cycles of six hybrid input-output subcycles and four error reduction subcycles and support constraint from optimal (least area) intersection of two offset autocorrelation masks from one hundred speckle patterns with expansion by factor of sixteen: control case (top left), point sampled case (top right), and integrating  $4 \times 4$  (middle left),  $8 \times 8$  (middle right),  $12 \times 12$  (bottom left), and  $16 \times 16$  (bottom right) squares of pixels in propagated image.*

the fill factor can be raised without seriously jeopardizing the robustness of the system.

Phase retrieval by the standard IFTA can be highly sensitive to the support constraint. Fortunately, a number of methods for selecting tight support constraints are available. Additional investigation into techniques for selecting the best achievable support constraint is clearly needed. These techniques may include selection between several different rules defining permissible support constraints.

This investigation did not explore phase retrieval in the presence of shot and other noise. The effect of noise on the quality of reconstructed images should also be investigated when additional funding is available.

### 3 Subaperture Design

#### 3.1 Derivation of Wavelength-Dependent Merit Functions

In this section a set of merit functions to evaluate candidate operational wavelengths is derived. The merit functions are general and are not tied to specific missions or atmospheric models.

In the case of low signal levels it is easier to understand results when they are expressed in terms of the number of photons at the detector. Thus, the signal to noise ratio is written as

$$SNR = N_s \sqrt{\frac{\eta}{N_s + N_b + N_d}}, \quad (9)$$

where  $\eta$  is detector quantum efficiency,  $N_s$  is the number of signal photons,  $N_b$  the number of background photons, and  $N_d$  the number of photons equivalent to the detector system electrical noise. The expressions for the number of signal, background, and detector noise events are

$$N_s = E_0 \frac{\lambda T_a^2 \rho_t^2 A_t D_r^2 T_r}{2\pi h c R^4 \theta_t^2}, \quad (10)$$

$$N_b = \frac{\pi^2 \lambda T_r L_b \Delta \lambda \theta_r^2 D_r^2}{32 B h c}, \quad (11)$$

$$N_d = \frac{1}{4B} \left[ NEP \frac{\lambda}{h c} \right]^2, \quad (12)$$

where

$\lambda$  = wavelength (m),

$E_0$  = transmitter energy per pulse (J),

$T_a$  = atmospheric transmission,

$\rho_t$  = target diffuse reflectivity,

$A_t$  = target area (m<sup>2</sup>),

$D_r$  = receiver collection lens diameter (m<sup>2</sup>),

$T_r$  = transmission of receiver optics,

$R$  = target range (m),

$\theta_t$  = transmitter full angle divergence (radians),

$B$  = pulse/detector bandwidth (Hz),

NEP = detector noise equivalent power ( $\text{W}/\sqrt{\text{Hz}}$ ),

$\Delta\lambda$  = receiver optical filter bandwidth ( $\mu\text{m}$ ),

$L_b$  = sky background spectral radiance ( $\text{W}/\text{sr}\cdot\text{m}^2\cdot\mu\text{m}$ ).

We now consider the signal-to-noise ratio as a function of wavelength. The atmospheric transmission, atmospheric spectral radiance, detector quantum efficiency, and NEP are all strong functions of wavelength. Thus from equations (10)-(12):

$$N_s \propto \lambda T_c^2, \quad (13)$$

$$N_b \propto \lambda L_b, \quad (14)$$

$$N_d \propto \text{NEP}^2 \lambda^2. \quad (15)$$

There are three cases of interest which can be derived from equation (9). The signal-limited case occurs when the number of signal photons is much larger than background or detector noise. In this case, referred to as "signal shot noise limited", the signal-to-noise ratio is equal to  $\sqrt{\eta N_s}$ . A merit function is derived by substituting equation (13) into the expression for signal-to-noise ratio and setting the background and detector terms to zero yielding

$$M_s(\lambda) = T_a(\lambda) \sqrt{\lambda \eta(\lambda)}. \quad (16)$$

A second case of interest occurs when background is present, but detector noise is negligible. Equation (9) can be expressed as

$$\text{SNR} = \sqrt{\frac{\eta N_s}{1 + N_b/N_s}}. \quad (17)$$

This expression approaches the signal shot noise limit as the background to signal ratio goes to zero. Thus a good merit function (where large values are desirable) to evaluate background effects is  $N_s/N_b$ . The larger the value of the background merit function, the easier it is to approach signal-limited operation. From equations (13), (15), and (17) a wavelength-dependent merit function with background present is

$$M_b(\lambda) = \frac{T_a^2(\lambda)}{L_b(\lambda)}. \quad (18)$$

The third special signal-to-noise ratio case occurs when background is negligible, but detector noise is present. In a manner analogous to the background-limited case, a merit function including detector noise effects is

$$M_d(\lambda) = \frac{T_a^2(\lambda)}{\lambda \text{NEP}^2(\lambda)}. \quad (19)$$

### 3.2 Evaluation of Wavelength-Dependent Merit Functions

Each of the new wavelength-dependent merit functions will be evaluated in this section. Atmospheric transmission is a factor in all three merit functions. The atmospheric transmission as a function of wavelength was evaluated using the current version of a standard atmospheric modeling program, LOWTRAN 7. The LOWTRAN parameters[8] were set up for noon, in midsummer (day 180) on a standard clear day (23 kilometer visibility), looking from sea level to space through a maritime aerosol atmosphere including the effects of multiple scattering. LOWTRAN 7 was used to evaluate both sky spectral radiance and transmission for wavelengths of 0.5 to 1.1  $\mu\text{m}$  over a series of elevation angles from 10 to 80 degrees above the horizon, in 10 degree increments. Figure 16 plots three of the cases showing atmospheric transmission as a function of wavelength at 10, 30, and 30 degrees above the horizon. The key features of these plots are as follows

1. The trend is toward higher transmission at longer wavelengths. For example, transmission 30 degrees above the horizon is 39 percent at 532 nm and increases to 64 percent at 1060 nm.
2. Strong molecular absorption from 750 to 770 and 920 to 970 nm make operation at these wavelengths undesirable.
3. The attractiveness of long wavelength operation becomes greater at low elevation angles. For example, the ratio of transmission at 1060 nm to transmission at 532 nm is 1.28 looking 80 degrees above the horizon, while it is 3.95 looking 10 degrees from the horizon.

#### 3.2.1 Signal Shot Noise Limit

In the shot noise limit it is desirable to maximize wavelength, quantum efficiency and atmospheric transmission. Figure 17 plots the quantum efficiency of four different, commercially-available detectors. The bialkali photomultiplier (PMT) is a Hamamatsu R268 tube chosen because it is an inexpensive device. The gallium-arsenide PMT (Hamamatsu R636) has extended red performance, allowing operation out to about 850 nm. The silicon photodiode (EG&G YAG-040) device has been chosen for operation at slightly longer wavelengths than standard

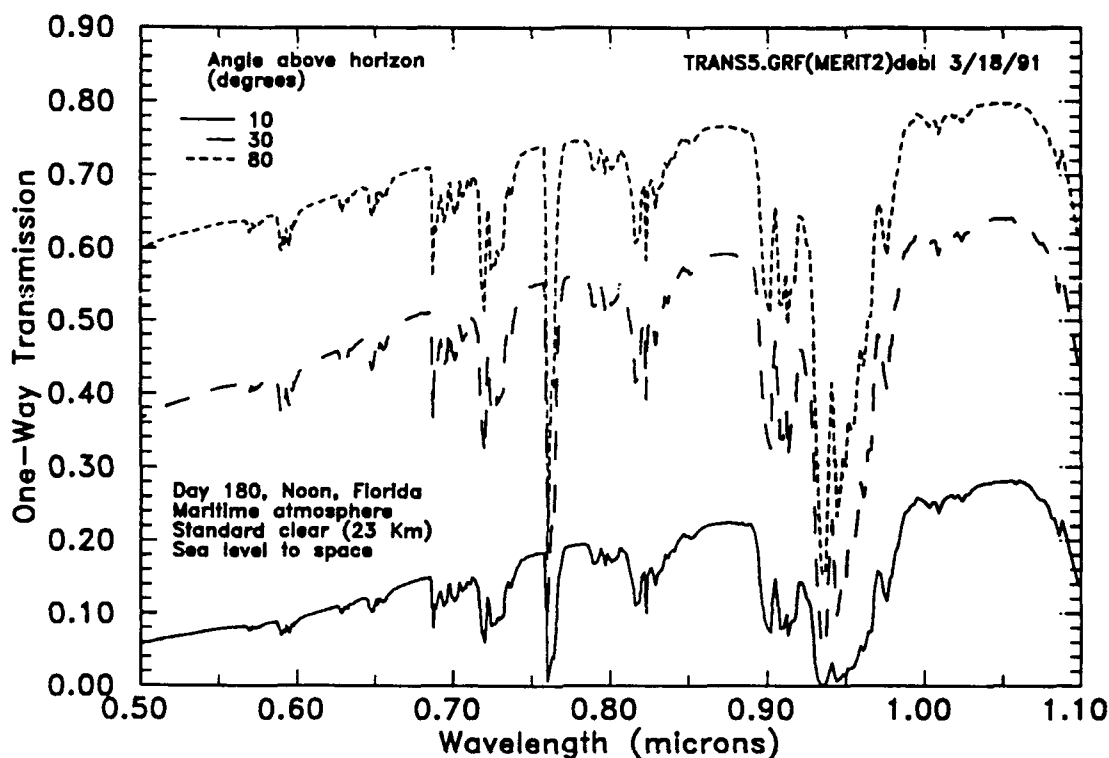


Figure 16. Atmospheric transmission versus wavelength.

silicon detectors to permit operation at Nd:YAG wavelengths. Finally, an ANTEL indium-gallium-arsenide avalanche photodiode (APD) detector designed for high speed fiber optics communications at 1.3 and 1.5  $\mu\text{m}$  is shown.

Several points should be noted with respect to detectors. First, the quantum efficiency of solid state detectors is much higher than photomultiplier tubes over the wavelength range of interest. Second, Nd:YAG wavelengths (1060 nm) fall near the long wavelength silicon edge and the short wavelength indium-gallium-arsenide edge. Finally, these curves do not show detector and amplifier noise which is considerably higher for APD and photodiode devices than for photomultipliers. Photomultiplier tubes provide nearly noise free gain on the order of a million. This noise free gain means PMT amplifiers operate with relatively large currents and are straightforward to design and operate. APD and photodiodes are noisy devices with low gain in the APD case ( $\approx 100$ -300) or no gain in the photodiode case. Furthermore, the APD has excess noise that often is 3-5 times larger than a PMT, while photodiode dark currents are typically much higher than PMT dark currents. The combination of low gain and high noise makes amplifier design and operation more difficult for solid state detectors. Active temperature control or compensation is required for solid state detectors.



Convenient lasers operating in the 0.5 to 1.1  $\mu\text{m}$  region are Nd:glass operating at 1060 nm, Alexandrite at 780 nm, Ruby at 694 nm, Rhodamine 6G near its peak at 590 nm, and frequency-doubled Nd:YAG at 532 nm. All of these wavelengths have the possibility of high power pulsed operation in the 1 to 50 Joule per pulse range. The merit functions have been evaluated over the range of 500 to 1100 nm.

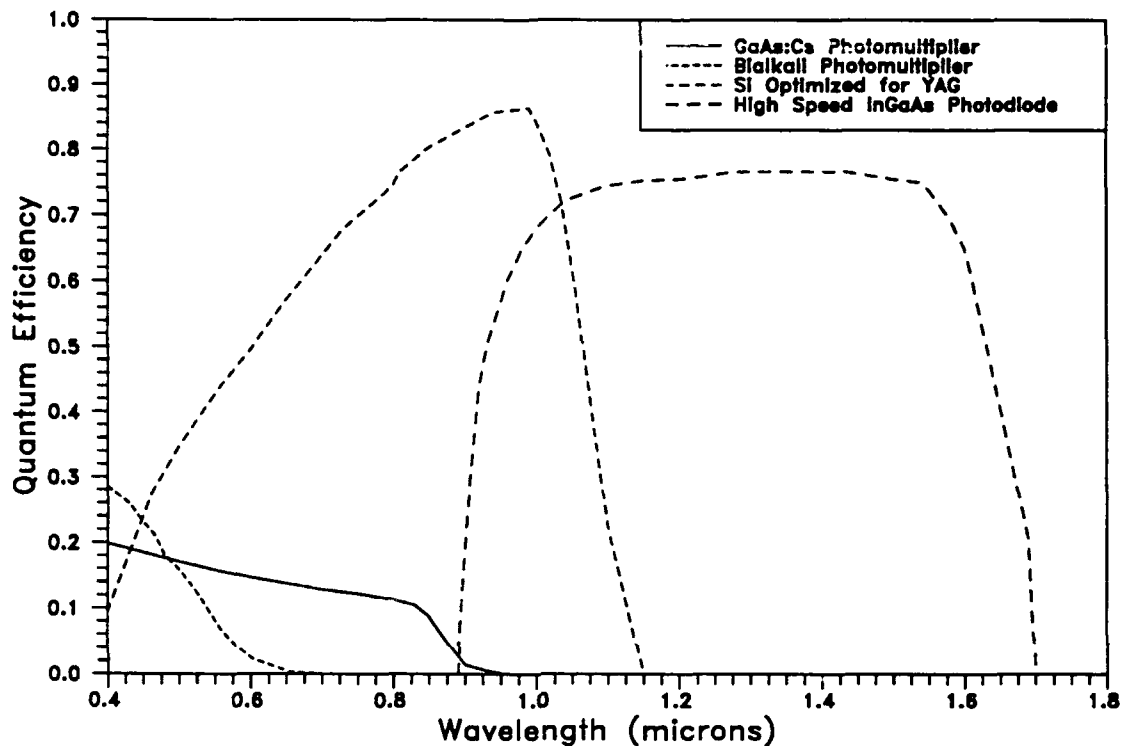


Figure 17. Quantum efficiency versus wavelength for various detectors.

The atmospheric transmission increases with wavelength due to decreased molecular scattering. Thus, multiplying transmission by a monotonically increasing function of wavelength yields a function which increases at longer wavelengths. Figure 18 plots  $M_s$ , the signal shot noise limited merit function. This merit function applies to the highest performance case when the detector is noise free and optical background has been totally suppressed. It shows a large performance advantage at longer wavelengths. Comparing Nd:YAG with frequency-doubled Nd:YAG, looking near vertical, the merit function is twice as large at long wavelengths. This advantage becomes larger as the mission requires operation closer to the horizon. At 10 degrees above the horizon the ratio is 7. Missions requiring low light level detector performance should be done at longer wavelength based on this merit function. For example, at 10 degrees elevation a system with a signal-to-noise ratio of 20 at 1060 nm would have a signal-to-noise ratio of 2.8 at 532 nm.

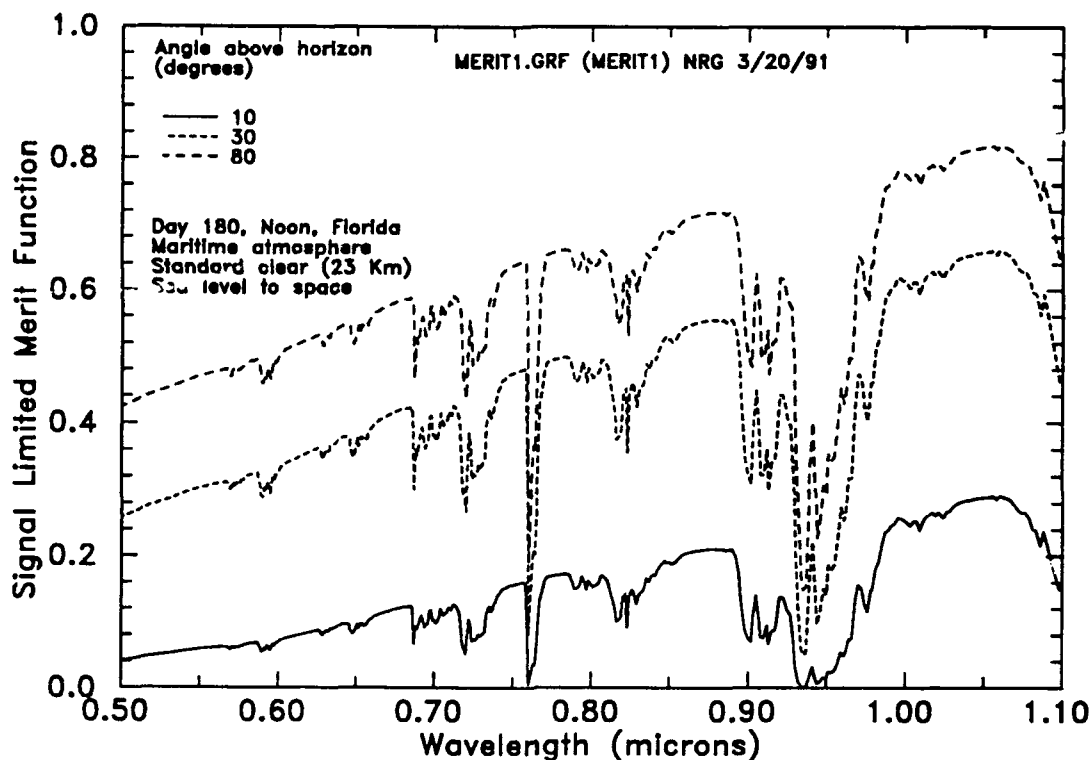


Figure 18. Signal-limited merit function versus wavelength.

### 3.2.2 Background Noise-limited Merit Function

The background noise-limited merit function is

$$M_b(\lambda) = T_a^2(\lambda)/L_b(\lambda). \quad (20)$$

The sky spectral radiance is required to evaluate this merit function and was computed using the same LOWTRAN 7 parameters as the atmospheric transmission. The background,  $L_b$ , is dependent on many parameters including atmospheric aerosols, elevation angle, and angle between the sun and system look vector. The spectral radiance is a weak function of the angle between the look vector and the sun when the angle is larger than 35 degrees as seen in Figure 19. At sun-look angles less than 35 degrees there is a rapid increase in sky spectral radiance. Thus 35 degrees sun-look angle is a convenient angle, because a system which has marginal background suppression at this angle will not function well at any angle. The large increase in background at 532 nm over 1060 nm should also be noted in Figure 19. The sky spectral radiance is plotted in Figure 20 for an angle of 35.5 degrees between the sun and look vector. The atmospheric conditions were the same as those used for computing transmission curves. The background is four to seven times higher at the shorter wavelength.

The merit function  $M_b$  was evaluated for a system with unit quantum efficiency detection, background radiance function shown in Figure 19 and the atmospheric transmission plotted in Figure 16. Figure 21 shows the background merit function normalized to one at an elevation angle of 10 degrees above the horizon and a wavelength of  $1.1 \mu\text{m}$ . These curves show the strong advantage of 1060 nm over shorter wavelengths since the merit function is about 50 times larger at long wavelengths. The conclusion that long wavelength operation is attractive based on the  $M_s$  merit function also is true based on the background merit function  $M_b$ .

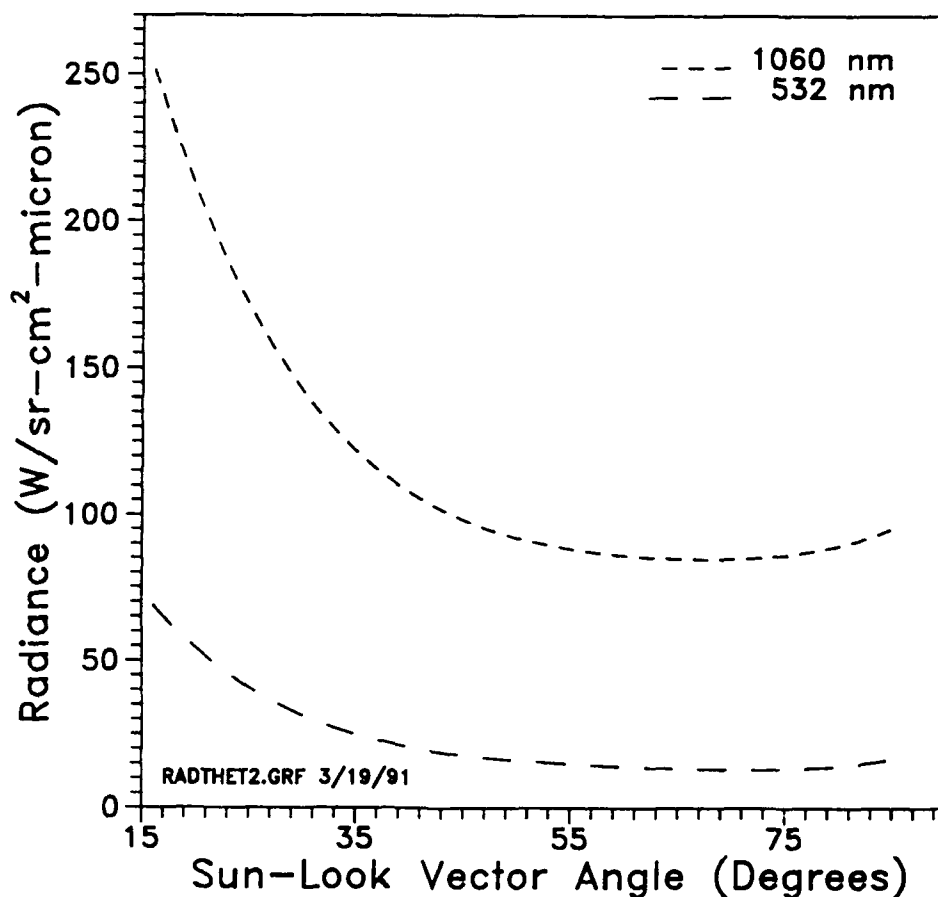


Figure 19. Sky radiance versus angle between the sun and look directions for Nd:YAG and frequency-doubled Nd:YAG.

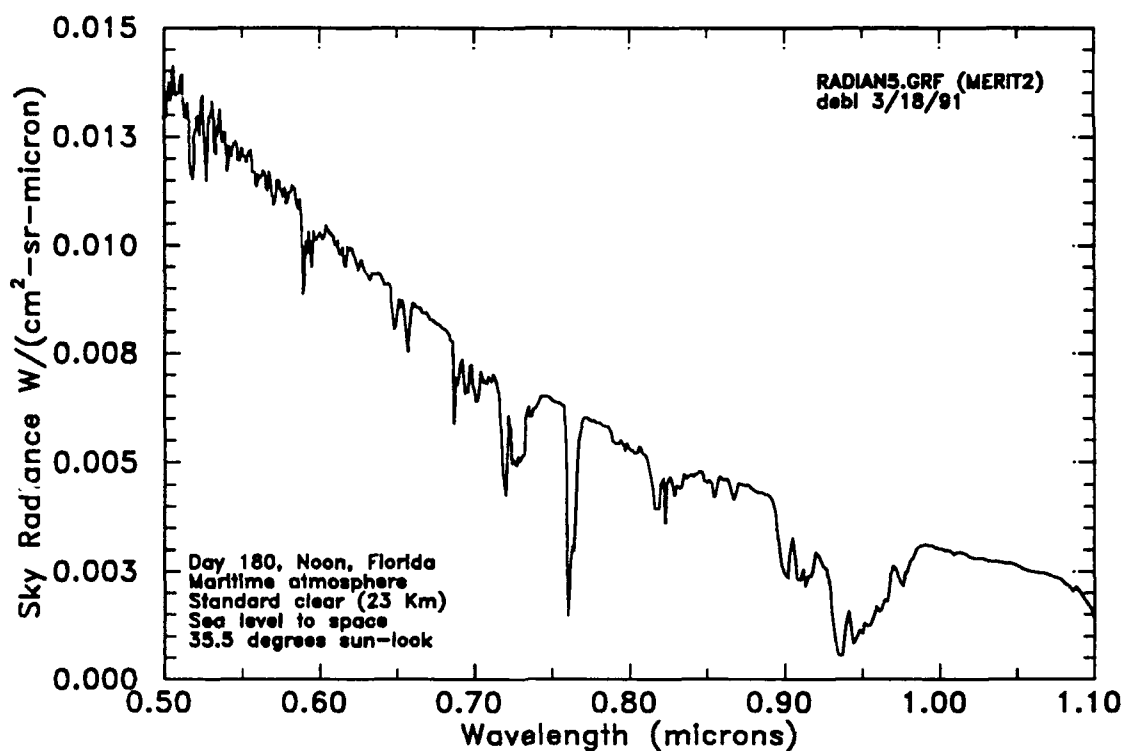


Figure 20. Sky spectral radiance versus wavelength.

### 3.2.3 Detector Noise-limited Merit Function

The detection-limited merit function is the ratio of transmission squared to wavelength as shown in Figure 22. At 80 degrees elevation angle  $M_d$  decreases slightly over the 500 to 1100 nm range changing from 0.72 at 532 nm to 0.61 at 1060 nm. At a 30 degree elevation the trend is reversed and the merit function increases slightly. At low elevation (10 degrees) the merit function is higher by factors of 5 at long wavelengths. The key point to note is that in the detector-limited case, assuming comparable NEPs, there is little difference between long and short wavelengths except at low elevation angles where long wavelength is clearly preferable.

The one caveat in this conclusion is the noise characteristic of a high quantum efficiency detector at 1060 nm. Off-the-shelf solid state detectors operating at room temperature are noisy compared with photomultiplier tubes, with NEPs on the order of than  $4 \times 10^{-14} \text{ W}/\sqrt{\text{Hz}}$ . This issue will be discussed in the next section.

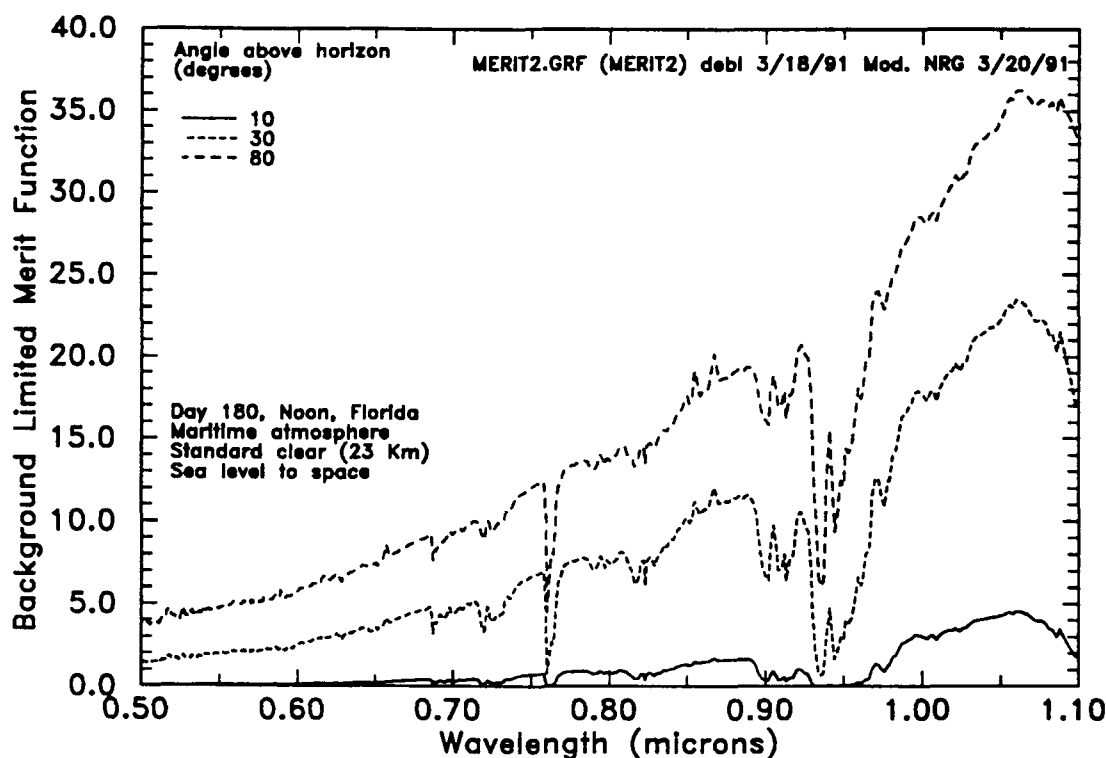


Figure 21. Background limited merit function versus wavelength.

#### 3.2.4 Subaperture Signal-to-Noise Ratio

The merit functions indicate that 1060 nm is a desirable wavelength at which to design a long-range imager operating in the atmosphere. In this section signal-to-noise ratio will be computed for a variety of detectors and compared with performance at a shorter wavelength. The comparison wavelength chosen is 590 nm, which is the peak output wavelength for commonly used R6G dye lasers. 590 nm is a slightly better wavelength than 532 in terms of atmospheric transmission and sky brightness. The purpose of these calculations is to verify that the case for operation at Nd:YAG wavelengths based on merit functions is correct and to estimate performance for a typical long range mission.

The number of photons falling on a 5 cm diameter circular aperture for a particular mission scenario is plotted in Figure 23. The mission-specific parameters used for signal-to-noise calculation are presented in Table 1. The conclusions with respect to wavelength choice are not mission-specific, because the differences are entirely due to atmospheric transmission and energy per photon. An elevation angle of 50 degrees was chosen so that the long path to space at shallow angles would not unduly bias the calculation. Operation at 1060 nm has an advantage of nearly ten times as many photons arriving at the detector compared with 590 nm,

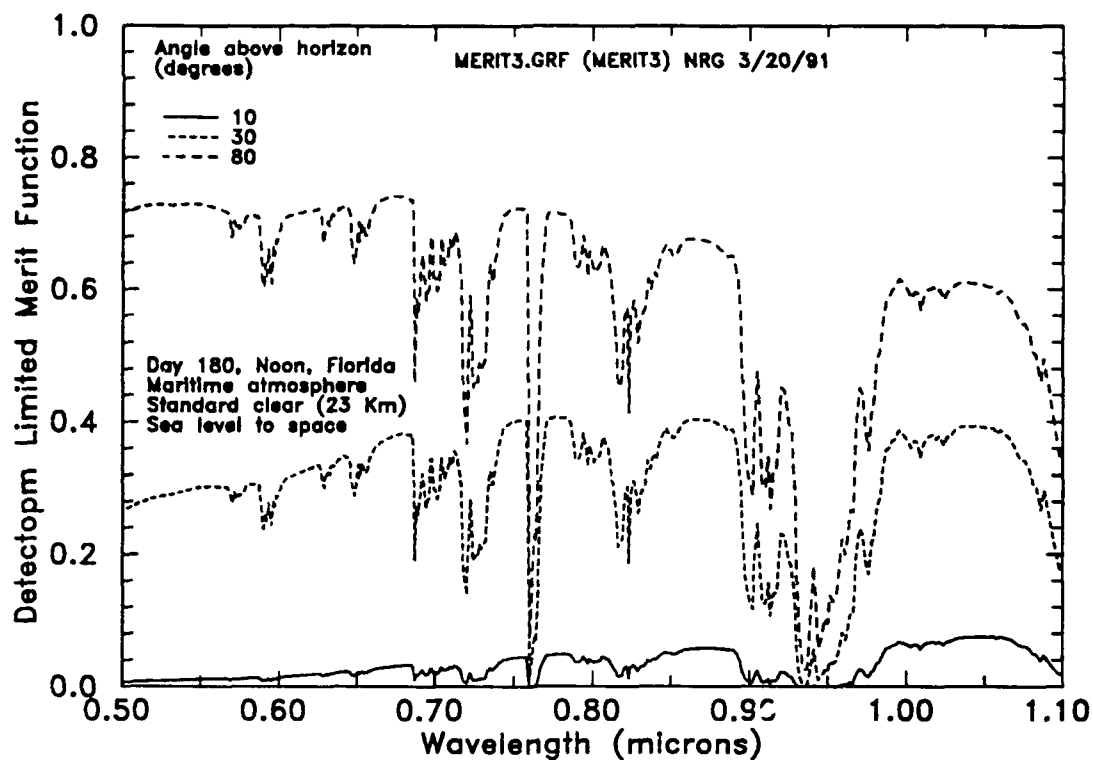


Figure 22. Detection limited merit function versus wavelength.

Table 1. Parameters for Signal-to-Noise Ratio Calculations

Parameter	Value
Energy/pulse	10 J
Pulse length	50 ns
Transmitter divergence	7 $\mu$ R
One-way atmospheric transmission	0.746
Target area	3 m <sup>2</sup>
Target diffuse reflectivity	0.3
Receiver transmission	0.7
Receiver diameter	5 cm
Receiver integration time	50 ns
Receiver FOV	1 mR
Optical bandwidth	3 nm

even on a clear day and at elevation angles far above the horizon.

Since signal-to-noise ratio includes background which has been shown to be several times lower at long wavelength, the signal-to-noise ratio is much higher

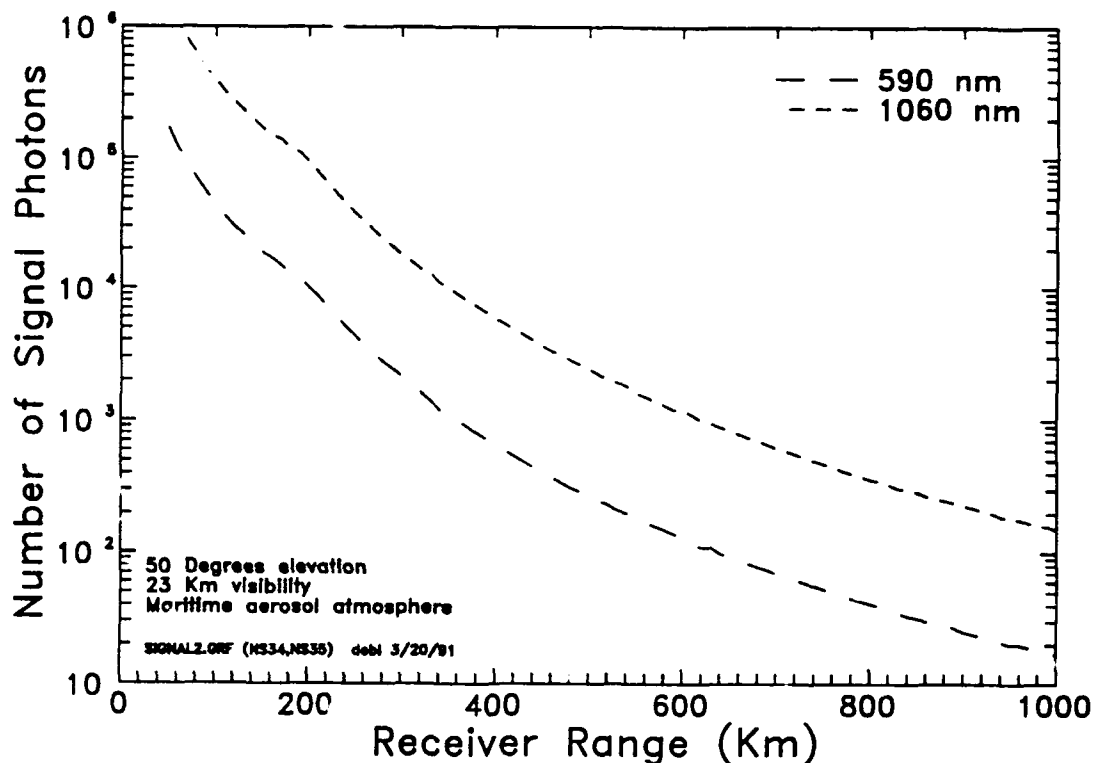


Figure 23. Number of signal photons versus range.

at long wavelength. This point is clearly shown in Figure 24, which plots signal-to-noise ratio based on NEP of existing detectors and an ideal noise free detector (NEP equal to zero). The signal-to-noise ratio based on existing detectors, as expected, is better at the longer wavelength. An even more significant point is that the ideal, noise free detector at 590 nm has a signal-to-noise ratio lower than that from an existing detector at 1060 nm. Thus, the advantage from improved transmission and lower background at long wavelength cannot be overcome by the use of better detectors at a shorter wavelength in a very reasonable example which does not have extreme elevation angles or haze, both of which increase the long wavelength advantage.

The signal-to-noise ratio performance of a system at 1060 nm utilizing various off-the-shelf detectors, with quantum efficiencies plotted previously in Figure 17, is shown in Figure 25. The NEP and quantum efficiency used in computing these curves are from catalogs for currently available devices. The indium-gallium-arsenide and silicon photodiode curves cross, because at high signal to noise the high quantum efficiency of the indium-gallium-arsenide (0.61) dominates over the silicon (0.38). The indium-gallium-arsenide detector is much noisier than the photodiode so that at long range, where signal levels are low, detector noise limits

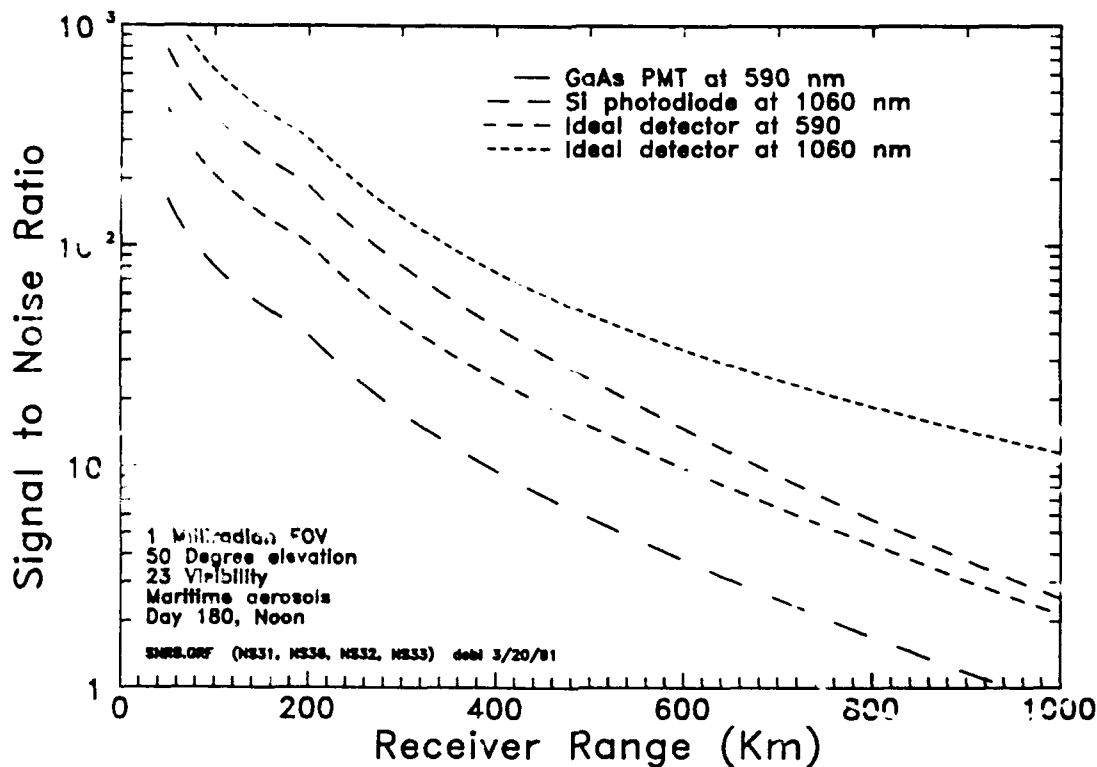


Figure 24. Comparison of existing and ideal detector at short and long wavelengths.

the signal-to-noise ratio. The only caveat in these results is that amplifier noise outside of the detector package is assumed negligible. In the case of the lowest NEP detector: which is a silicon photodiode, there is no internal gain. This means the amplifiers must have extremely low-noise and high gain, which makes the electronics design difficult.

Figure 26 is a what-if graph, plotting signal-to-noise ratio with improved detectors. Table 2 presents current and improved performance of detectors. All the improvements in performance should be achievable with a detector development effort. In the case of the EG&G silicon APD, the NEP is improved from  $8 \times 10^{-14}$  to  $2 \times 10^{-15}$ . NEPs on this order have been reported at shorter wavelengths using improved amplifiers and selected devices. The improved ANTEL device assumes the NEP of the gallium-aluminum-arsenide APD is  $4 \times 10^{-15}$ , which will require device development. Finally, an improved silicon photodiode with a DC quantum efficiency of 0.50 instead of 0.38 and an NEP of  $4 \times 10^{-15}$  is postulated. A curve for a noise-free detector is plotted for comparison. The noise-free detector represents background-limited performance. The conclusion from these curves is that near background-limited performance should be possible with reasonable detector



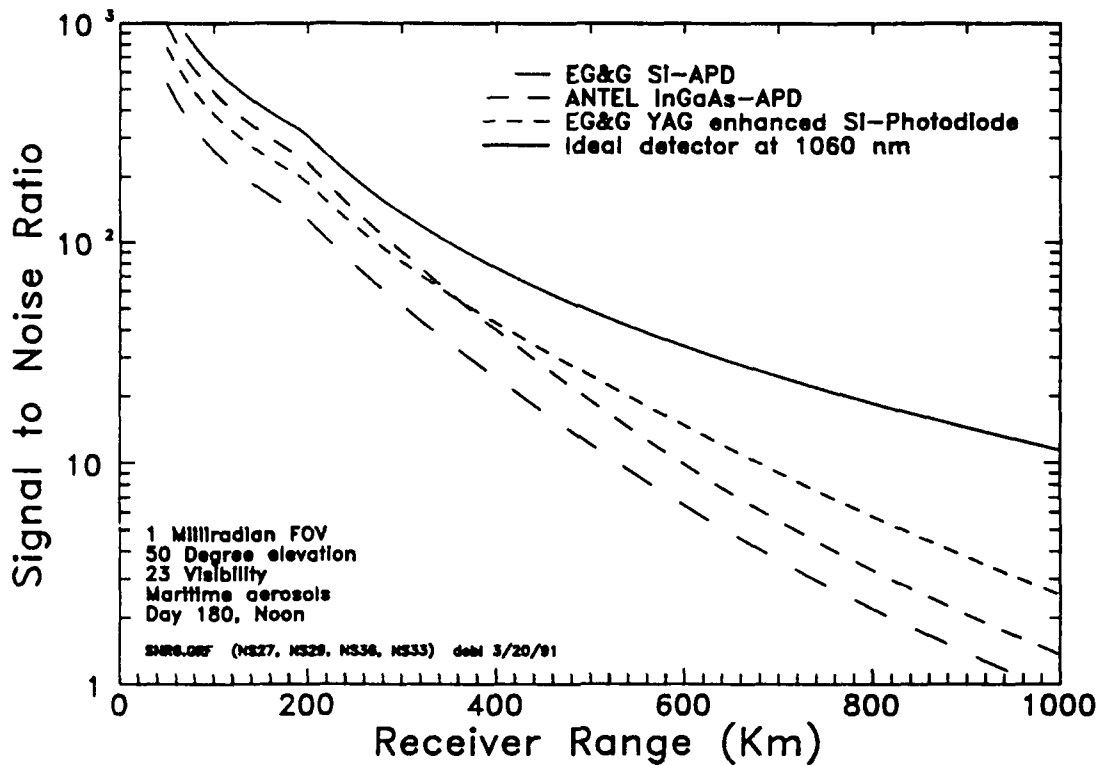


Figure 25. Comparison of signal-to-noise ratio using off-the-shelf detectors.

improvements. In this particular example a signal-to-noise ratio of 10 is achieved at 1000 Km range using a 10 Joule laser and 5 cm subapertures.

Table 2. Detector Parameters

Detector	Current		Goal	
	$\eta$	NEP ( $W\sqrt{Hz}$ )	$\eta$	NEP ( $W\sqrt{Hz}$ )
EG&G 30919E (Si-APD)	0.18	$8 \times 10^{-14}$	0.18	$2 \times 10^{-15}$
EG&G YAG-040	0.38	$4 \times 10^{-14}$	0.50	$4 \times 10^{-15}$
Antel (InGaAs)	0.61	$1 \times 10^{-13}$	0.61	$4 \times 10^{-15}$
Ideal detector	1.0	0		

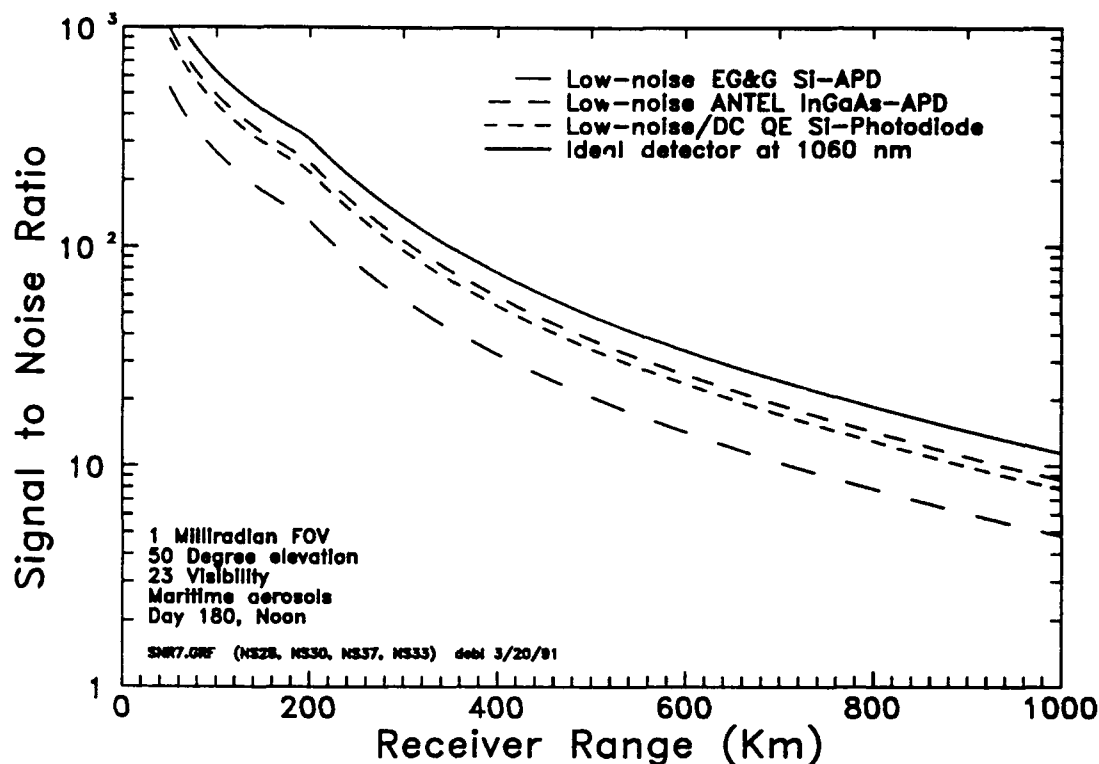


Figure 26. Comparison of signal-to-noise ratio using improved detectors.

### 3.3 Subaperture Design

The subaperture design considered here is for a fixed, narrow field-of-view device. The overall concept is to mechanically steer the subaperture assemblies, rather than trying to build each subaperture with a wide field-of-view. This choice reduces the subaperture complexity and allows subapertures to be built with no moving parts. Figure 27 shows a concept drawing of a subaperture. An optical system consisting of a lens and pinhole collects light over a narrow field-of-view. An interference filter centered on the laser illumination wavelength is placed near the focal plane to reduce optical background. A detector-amplifier combination is fed into a gated integrator. The integrator, which is controlled by a digital signal processor (DSP) control signal generated external to the subaperture, is turned on when light reflected back from the target falls on the array. The gated integrator output is digitized and read by a DSP controller over a digital interface.

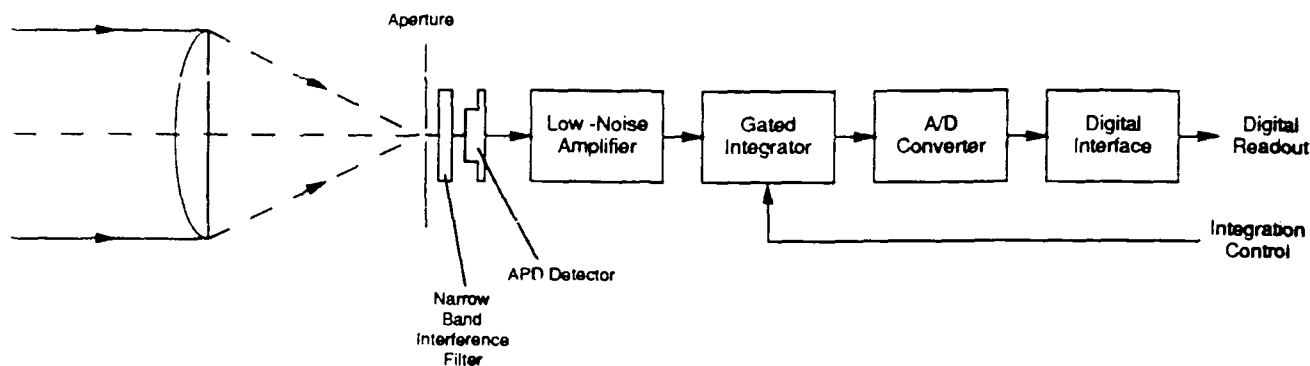


Figure 27. Schematic diagram of a subaperture.

### 3.3.1 Collection Optics

Lens design is an important part of the subaperture design. A diffraction-limited lens has a blur circle with angular diameter

$$\beta = \frac{2.44\lambda}{D},$$

where  $\lambda$  is the wavelength and  $D$  is the clear aperture. This means at a wavelength of  $1.06 \mu\text{m}$  with a 5 cm collection aperture a diffraction-limited system has an angular blur of 0.052 milliradians, which is 19 times smaller than the required one milliradian IFOV for daytime background suppression. Thus the required optical performance is limited by geometrical optical aberrations rather than the diffraction limit. A single element collection lens with spherical surfaces is desirable. The equations for geometrical aberrations (in radians) of a single-element lens bent to minimize spherical aberration are:

$$\text{spherical} = \frac{n(4n-1)}{128(n+2)(n-1)^2(F/\#)^3},$$

$$\text{sagittal coma} = \frac{\theta}{16(n+2)(F/\#)^2},$$

$$\text{astigmatism} = \frac{\theta}{2(F/\#)},$$

$$\text{sagittal field curvature} = \frac{\theta^2(n+1)}{(F/\#)2n}, \text{ and}$$

$$\text{tangential field curvature} = \frac{\theta^2(3n+1)}{(F/\#)^2n},$$

where  $n$  is the lens index of refraction,  $F/\#$  is the lens F number and  $\theta$  is the angular field-of-view. Table 3 gives angular geometric aberration-induced blur in milliradians for both low (BK7) and high index (SF6) elements for a one milliradian field-of-view, five centimeter diameter receiver. The narrow field-of-view system is dominated by spherical aberration, with small amounts of astigmatism present. The conclusion from this table is that a single element is adequate. The choice between high and low index glass is made on the basis of field-of-view. If the field-of-view is one milliradian, then a low index BK7 element will have spherical aberration equal to the field-of-view for an F/4 system. Thus, the lens chosen is an off-the-shelf plano-convex with a 200 mm focal length.

Table 3. Aberration Blur (in milliradians) for a 50 mm Diameter Singlet Bent to Minimize Spherical Aberration.

n	f(mm)	d <sub>pin</sub>	Sph.	Coma	Astig.	Field <sub>s</sub>	Field <sub>t</sub>
1.5	100	0.1	8.4	0.0	0.125	0.0	0.0
1.5	200	0.2	1.0	0.0	0.062	0.0	0.0
1.5	300	0.3	0.3	0.0	0.042	0.0	0.0
1.8	100	0.1	4.5	0.0	0.125	0.0	0.0
1.8	200	0.2	0.6	0.0	0.062	0.0	0.0
1.8	300	0.3	0.2	0.0	0.042	0.0	0.0

The overall length of the system is determined primarily by the optical system. A sunshade may need to be placed in front of the collection optics to restrict the background field-of-view to a narrow cone. The need for and length of the sunshade and its design will be evaluated during the experimental phase of the program.

### 3.3.2 Bandpass Filter

An optical thin film interference bandpass filter will be used to reduce sky background. The acceptance angle for such a filter is determined by the filter design. A high index spacer layer allows a larger field of view than a low index spacer. The shift in the center wavelength of the bandpass filter is given by the expression

$$\lambda = \lambda_0 \sqrt{1 - \left(\frac{\sin \theta}{N}\right)^2}, \quad (21)$$

where

$\lambda_0$  = bandpass center wavelength at normal incidence,

$\lambda$  = shifted bandpass filter center wavelength,

$\theta$  = angle of incidence on filter, and

$N$  = spacer layer index of refraction.

The index of refraction for commercially available Nd:YAG filters is 2.05. Figure 28 plots the center wavelength versus angle of incidence for a bandpass filter centered at 1060 nm at normal incidence. The wavelength shift is about 2 nm at 7.25 degrees, which means the filter will work in a convergent F/4 beam without a large transmission penalty. In the previous section a 3 nm bandwidth optical filter was assumed. A filter with a 3 nm bandpass is very practical as illustrated by the wavelength shift curve. The filter transmission will be in the range of 50 to 60 percent. Placement of the bandpass filter in the focal plane represents a significant cost savings for volume subaperture fabrication. The filter diameter is 5 mm in the focal plane, while it is 50 mm when it is located in front of the lens. This means a 100 fold reduction in filter area and a large cost savings, particularly for a narrowband device of the type required here.

### 3.3.3 Detector and Electronics

Detectors were discussed in the section on merit function evaluation. The lowest noise detector in Table 2 was a silicon photodiode, but low-noise amplifiers are a serious problem at very low optical intensity. The detector output will be a very low level signal with 100 photons incident on the detector. The silicon-APD with built-in preamplifier is chosen because uncooled amplifiers can be used which simplify the system. Furthermore, the performance at 1060 nm for this particular APD can be improved considerably by using better hybrid preamplifiers in the detector package. The NEP for the standard EG&G model 30919E silicon-APD at

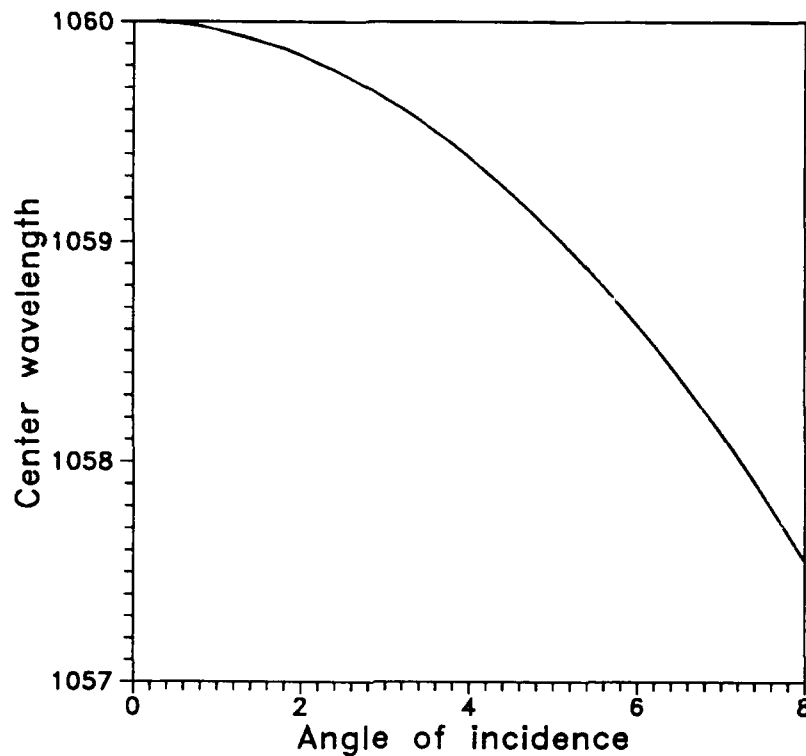


Figure 28. Central wavelength versus angle of incidence for a Nd:glass laser band-pass filter.

1060 nm is  $8 \times 10^{-14} \text{ W}/\sqrt{\text{Hz}}$ , but this number is pessimistic. Noise equivalent powers 20 to 30 times lower are available by cooling the detector with a TE cooler and selecting devices. This would allow detection with an SNR of 10 out to a range of 1,000 km. The electronics block diagram is shown in Figure 27. The detector/preamplifier output is amplified and fed into a gated integrator. A range gate from a central DSP turns on the integrator during the time light reflected from the target falls on the subaperture. An analog-to-digital converter digitizes the integrator output and makes it available to the data collection system on a digital bus.

#### 3.3.4 Subaperture Parts List

A subaperture parts list, together with low volume component cost estimates excluding non-recurring engineering costs, is given in Table 4. Non-standard parts are marked with stars to indicate prices are estimates. The bulk of the cost is for the detector and associated electronics. The low level signals require precision, low-noise components. For example, the power supply used for an APD must have much less ripple than PMT power supplies. Similarly, the amplifiers used with APDs must be much lower noise than those used with PMTs. This is the

penalty paid for using a detector with a gain on the order of  $10^2$  instead of  $10^6$ . Laboratory fabrication of a prototype APD with electronics is required to accurately estimate volume production cost.

This design is more expensive in low volume production than a previous agile subaperture concept. The cost can be reduced by several methods. First, volume production of the APD will reduce cost significantly. Second, cooling the APD and preamplifier will reduce noise and simplify the design, thus, use of active thermoelectric cooling will be studied in the detailed electronics design. The tradeoff is additional system complexity for thermal control versus lower cost amplifiers resulting in a lower system cost. Finally, for volume production a custom hybrid amplifier design will be considered for cost reduction. The cost of an APD detector without electronics is comparable to the cost of a PMT (less than \$300 single quantity), so the electronics design task is to determine the best way to reduce the electronics cost. It is expected that an APD with low noise amplifiers could be built in volume for \$600 to \$700 which is a 40 percent reduction in the single quantity cost. A similar reduction in the cost of other components in volume quantity (4000) leads to a subaperture comparably priced with the previous design[9], but having significantly improved performance.

### 3.3.5 Mechanical Design

The subapertures require three degrees of freedom for mechanical adjustment: focus and two-axis focal plane translation of the aperture-detector combination. Each of these degrees of freedom requires only small ranges. For example, the  $\pm 2$  percent range typical of lens focal length specification means 8 mm total focus adjustment is required for the 200 mm focal length optics. The two axis translation range will be 3.5 mm to allow a one degree angular FOV adjustment. A one milliradian field-of-view requires 0.1 milliradian pinhole location which implies a 20  $\mu\text{m}$  tolerance. Similarly, a 0.1 milliradian FOV error implies a maximum 80  $\mu\text{m}$  error in focal adjustment. Special purpose mechanical translation will be designed into the package as part of the detailed mechanical design. These are easily achieved mechanical ranges and tolerances. Each subaperture package will be assembled and aligned in a test fixture using the outside of the housing as a reference. The adjustments will be locked in place mechanically using set screws.

Once each subaperture is aligned it will be placed into the mechanical tracking system. Prealignment of individual subapertures assures interchangeability. There is no unique solution to subaperture array tracking. One choice for a subaperture steering concept is to use a radar pedestal or other large antenna steering unit to mount racks of subapertures. Pedestals capable of moving large radar dishes currently exist and are good candidates for up to 10 meter diameter arrays. The

Table 4. Narrow Field-of-View Subaperture Parts List

Part	Source	Cost
Biconvex lens	CVI BICX-50.0/205.2 p.112	\$110
Lens AR coating	CVI (qty. 8)	\$75
Bandpass filter	Andover 030FC38-25	\$100
FOV aperture	**	\$50
2-axis translator	**	\$100
APD	EG&G C30919E (qty. 1)	\$1160
Housing	**	\$50
Electronics		\$438
Power supply	**	\$200
Low-noise amp.	AD 9717+CLC501	\$37
Gated SH	discrete	\$50
A/D	Harris HI-7153	\$16
Interface	**	\$40
PCB	**	\$75
Connectors	**	\$20
TOTAL		\$2083

subaperture arrays are unphased and have alignment tolerances that are comparable to microwave antennae. The alignment tolerance depends on the field-of-view. It is required that all the subapertures look in the same direction, so the 0.1 milliradian field-of-view tolerance assumed for alignment of each subaperture carries over to the array. This implies a one millimeter tolerance over a 10 meter array which is on the order of  $10^4$  times larger than a telescope built from phased mirrors.

A second steering scheme is to mechanically link the subapertures venetian blind style. This has the advantage of allowing a fixed plate mounted rigidly to the ground instead of a steerable plate. It also has scalability advantages for systems larger than 10 meters where tracking mounts become very expensive. The details of two axis linkage schemes will be worked out during the detailed mechanical design and compared with the steerable antenna approach.



### 3.3.6 Lasers

The laser wavelength chosen is 1060 nm. Several high power candidate lasers operate near this wavelength, Nd:YAG at 1064, Nd:glass at 1060 and Nd:YLF at 1047 nm. We conclude that long wavelength operation is desirable and the system design considerations are independent of the particular laser illuminator chosen.

### 3.4 Summary of Subaperture Design

The approach to subaperture design described in this report differs in two basic ways from earlier work.[10] First, the subaperture is non-agile which simplifies the design. Second, the illuminator wavelength has been shifted to a longer value.

The advantages of a narrow fixed field-of-view over the previous agile design are as follows:

1. Small area, solid-state detectors can be used. Independent of wavelength, much higher quantum efficiency is available from a solid-state detector compared with a PMT.
2. The optical design is much simpler. The narrow field-of-view means a single element lens can be used, reducing optics cost and internal scatter.
3. No moving parts are required. This makes the subaperture rugged, simple, and easy to prealign.
4. Packaging is simplified and a system noise source (internal motors) is removed.

There are five advantages of long wavelength operation:

1. Lower background due to reduced sky spectral radiance.
2. Increased atmospheric transmission, which is particularly important in active imaging where the target must be illuminated through the atmosphere. This means transmitter power can be reduced an order of magnitude over a comparable shorter wavelength system.
3. Higher quantum efficiency detectors are available.
4. Increased number of photons per Joule of laser power. This is a small advantage compared with the others, but it is still a factor of two changing from 532 to 1060 nm.
5. Simplified boresighting because of the larger field-of-view. Operation at shorter wavelength requires a narrower field-of-view to reduce the background. This in turn means tighter mechanical tolerance on most components.

## 4 Key Issues for Phase Retrieval Algorithms

This section discusses key issues which must be addressed to verify that existing or proposed phase retrieval algorithms will be able to satisfy system requirements for a wide variety of targets and backgrounds. In each case, a strawman approach to resolving the issue has been identified.

### 4.1 Direct Phase Retrieval from Single Speckle Patterns

This section discusses improvement of the image quality achievable by processing an ensemble of sampled speckle pattern intensities to obtain a series of speckle images which are then averaged.

The original correlography method developed independently by SPARTA, and a team from AFWL, and ERIM relied on averaging the autocorrelations computed from individual speckle patterns. This algorithm proceeds counterclockwise from an ensemble of detected speckle patterns to a reconstructed image as shown in the flow chart in Figure 29. This averaging process has the effect of reducing the signal to noise of the high spatial frequency components in the reconstructed image. A new process developed by SPARTA uses the image produced by standard correlography as the starting point and produces reconstructed images with image quality limited primarily by the number of detected photons in the ensemble of speckle patterns. This algorithm proceeds clockwise from a single detected speckle pattern in the flow chart shown in Figure 29. This new process reconstructs an image from each detected speckle pattern and then aligns and averages the results.

A key requirement for direct image reconstruction from a single speckle pattern is the existence of a tight support constraint. We should examine the ability to generate tight support constraints using three techniques: iterative derivation using correlography followed by image thresholding, minimum area support constraints derived from the averaged autocorrelation, and a triple intersection algorithm using the averaged autocorrelation. The iterative derivation has been examined by Lees and Henshaw.[11] The minimum area algorithm has been proposed by Norm Guivens of SPARTA. Finally, the triple intersection algorithm has been investigated by J. Fienup of ERIM.[12]

### 4.2 Phase Retrieval Performance for Low SNR

Long range active imaging systems will always tax the requirements for the laser illuminator. As a result, the sampled speckle patterns will tend to have a small number of detected photons per speckle pattern per subaperture. In theory, the most effective use of laser photons for correlography is achieved with an average of one detected photon per speckle pattern per subaperture.[13] The effect of background leakage and detector noise will rapidly degrade the achievable image quality.

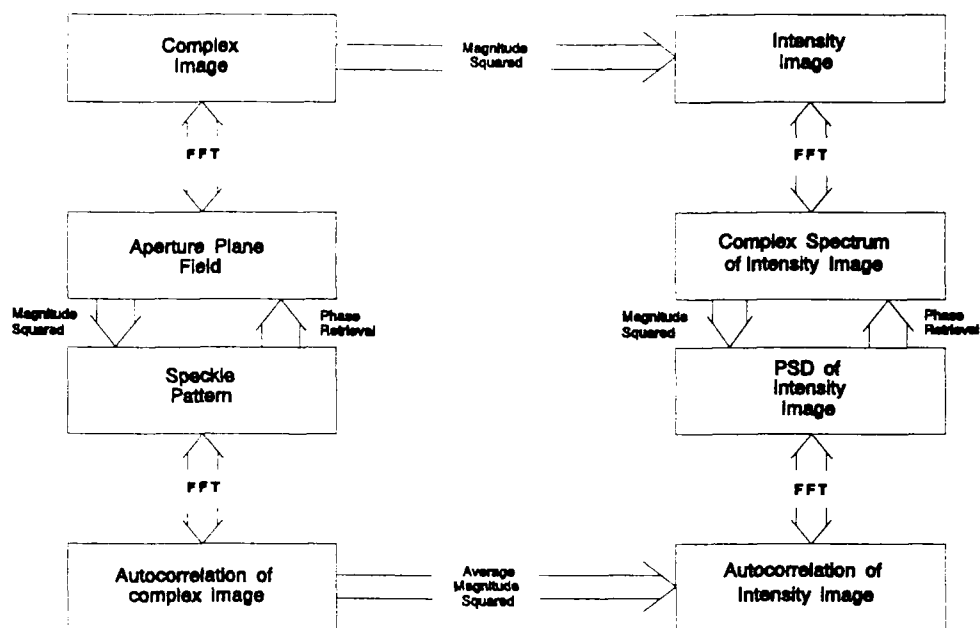


Figure 29. Flow chart for image reconstruction from sampled speckle pattern intensities.

The effects of low photon count, background leakage, and detector noise can be studied using SPARTA's high fidelity active sensor simulation, SENSORSIM. This unique simulation can produce speckle patterns with theoretically correct speckle statistics.[14] A detector model funded by SDIO and currently under development will permit the inclusion of detailed detector noise effects for a wide range of subaperture detection systems.

#### 4.3 Target Parameter Influence on Phase Retrieval

Phase retrieval is known to work well for certain classes of targets, specifically targets consisting of several spatially separated objects, and targets with a large amount of high spatial frequency content. The concern is that certain types of targets will be especially difficult to image using phase retrieval techniques. In addition, target rotation can blur the detected speckle pattern during a finite exposure time. If this exposure time is too short, however, the transform-limited illumination coherence will be too small to produce a well-developed speckle pattern. It will be important to quantify these limits in terms of target diameter, rotation rate, and range.

It is important to study the ability to reconstruct targets of three specific types: highly symmetric targets, targets with a small number of glints, and targets with non-stationary glints. Fienup has suggested that highly symmetric targets will be

difficult to reconstruct using phase retrieval techniques.[15] Elbaum has suggested testing phase retrieval with the other two classes of targets during ISTEf Science Advisory Committee meetings.[16]

#### 4.4 Investigation of the "Zero-lag" Problem

The zero-lag term of the image autocorrelation is the central value, which is always the maximum value for real-valued targets. This term corresponds to a pedestal term in the image power spectral density and thus affects every point of the PSD used in the phase retrieval process.

Direct calculation of the zero-lag term of the target autocorrelation derived from an ensemble of speckle patterns results in extremely slow convergence to the correct value. In principle, this problem can be solved iteratively by assuming a value for the zero-lag term, performing a reconstruction, recording the residual mean-squared error, then changing the zero-lag estimate and repeating the process. The proper zero-lag value is determined using a hill-climbing technique. However, this method would be extremely computationally intensive. SPARTA has devised a method which provides much faster convergence for the case of "gaussian" targets, i. e., targets with diffuse surfaces.[17] It will be important to investigate the convergence of this method to the correct value for targets which are not entirely diffuse.

The zero-lag problem does not exist for the direct image retrieval from a single speckle pattern. However, iterative derivation of the support constraint as described above cannot be performed if the zero-lag problem cannot be solved. Thus the importance of this problem depends on the results of examining the minimum area and triple intersection methods for determining a tight support constraint.

#### 4.5 Alternative Phase Retrieval Methods

Different phase retrieval techniques may be complementary in the sense that images which are difficult to reconstruct using one technique may be easier to reconstruct with another technique. Two methods which should be investigated in this context are triple correlation and the exponential wedge algorithm. The key initial question to be considered is whether these algorithms can be applied to the sampled intensity of speckle patterns reflected from a laser-illuminated object.

#### 4.6 Subaperture Design

During previous work, SPARTA has identified several key issues associated with subaperture design. These issues are cost, background suppression capability, detector NEP (at  $1.06 \mu\text{m}$ ), and co-boresighting of an array of apertures.

Cost is a key consideration since as many as 4000 subapertures may be needed for high quality imaging systems. If cost were no object, the construction of photon counting subapertures with high background suppression is clearly possible. The goal is to achieve this performance with low cost subapertures.

The results of algorithm investigations will establish limits on the background leakage and detector noise which can be tolerated in a multiple aperture imaging system. Based on these limits, it will be possible to re-examine two existing subaperture designs we have already developed, one for an agile subaperture to be placed on a fixed mount and one for a fixed field of view subaperture which could be placed on an agile mount.

A summary of these issues associated with phase retrieval algorithms is shown in Table 5.

Table 5. Summary of Key Issues for Phase Retrieval

1. Direct phase retrieval from single speckle patterns
  - 1.1 Support constraint investigations
    - Iteratively derived support constraint
    - Minimum area constraint
    - Fienup constraint
2. Phase retrieval performance for low SNR
  - 2.1 Low photon count
  - 2.2 Single speckle image
  - 2.3 Background leakage
  - 2.4 Detector noise
3. Target parameter influence on phase retrieval
  - 3.1 Limits on target size, rotation rate, and range
  - 3.2 Phase retrieval in presence of small numbers of glints
  - 3.3 Phase retrieval for nonstationary targets
4. Investigation of the "zero-lag" problem
  - 4.1 Investigation of the "hill-climbing" method
  - 4.2 Investigation of the "gaussian target" method
5. Alternative phase retrieval methods
  - 5.1 Triple correlation
  - 5.2 Walker algorithm (exponential wedge)
6. Subaperture design
  - 6.1 Electronics
  - 6.2 Co-boresighting assembly

## 5 Conclusions

All three key issues listed in the Introduction for the development of a multiple aperture imaging system have been addressed in this report. The key issues fall into three areas:

1. Can a photon-counting subaperture be built for a reasonable cost so that a large array is affordable?
2. Can an array of subapertures collect the information required to form an image?
3. Is the algorithm used to perform phase retrieval from the intensity measurements suitable robust given the quality of detected speckle intensity data?

We have concluded that a satisfactory subaperture design is possible, and that the best wavelength for imaging through the atmosphere to space is near  $1.06\mu\text{m}$ , the wavelength of a Nd:YAG laser. The design discussed in this report is not agile, but instead can be used to track a single object with a suitable array mount. An agile design at  $1.06\mu\text{m}$ , should also be developed.

The most important array issue addressed was the permissible value of the fill factor. We determined that linear fill factors greater than 50% are allowable, which will permit the design of a photon-efficient collecting array. The remaining tasks will involve array mount design to achieve receiver tracking capability or agility. For example, the array may be mounted on a telescope mount or may involve individual mounts for each subaperture.

Finally, we have discussed the key issues for phase retrieval algorithms. Many of these issues will be solved by the ability to generate a tight support constraint. We have already shown that with a tight support constraint, direct retrieval of images from single speckle patterns is possible. This direct retrieval process will allow high-signal-to-noise images to be produced from a series of detected speckle patterns and will eliminate the zero-lag problem. Improved algorithms using a tighter support constraint will need to be tested for a wide variety of targets and backgrounds, and the performance will need to be evaluated in the presence of detector and background noise.

## References

1. P.D. Henshaw and D.E.B. Lees, "Electronically agile multiple aperture imager receiver," *Opt. Engineer.* **27** (1988) 793.
2. D.E.B. Lees, R.F. Dillon, P.D. Henshaw, D.P. DeGloria, J.M. Rota, D. Wyschogrod, and R.C. Knowlton, "Demonstration of Speckle Imaging of 3D Targets Using Pulsed Illumination," *IRIS Active Systems* (Boulder, CO, 1988).

3. P.D. Henshaw, D.E.B. Lees, and R.F. Dillon, "Laser speckle data collection experiments," *Proc.SPIE* **1351** (1990) 616.
4. M. Abramowitz and I. Stegun, Eds., *Handbook of Mathematical Functions with Formulas, Graphs, and Mathematical Tables*, National Bureau of Standards, U. S. Department of Commerce, Washington, DC, 1970, p. 940.
5. J. W. Goodman, *Statistical Optics*, John Wiley & Sons, New York, 1985.
6. J. W. Goodman, "Statistical Properties of Laser Speckle Patterns," in J. C. Dainty, Ed., *Topics in Applied Physics* Vol. 9, Springer-Verlag, New York, 1984.
7. J. R. Fienup, "Phase Retrieval from Fourier Intensity Data," *Digital Image Recovery and Synthesis*, *Proc. SPIE.* **828** (1987), p. 13
8. F. X. Kneizys, et. al., "Users Guide to LOWTRAN 7," AFGL-TR-88-0177, August 16, 1988.
9. D.E.B.Lees and R.F. Dillon, "Agile Multiple Aperture Imager Receiver Development - Final Report," SPARTA LTR 90-001, (February 15, 1990).
10. D. E. B. Lees and R. F. Dillon, "Agile Multiple Aperture Imager Receiver Development - Final Report," SPARTA LTR 90-001, (February 15, 1990).
11. D. E. B. Lees, and P. D. Henshaw, "A New Method for Direct Image Recovery from Speckle Patterns," 1989 OSA Annual Meeting, Orlando, FL (October, 1989).
12. T. R. Crimmins, J. R. Fienup, and B. J. Thelen, "Improved bounds on object support from autocorrelation support and application to phase retrieval," *J. Opt. Soc. Am.* **A7** 3 (1990).
13. P. D. Henshaw and N. R. Guivens Jr., "An Imaging System Performance Metric," SPARTA White Paper, 3 December 1990.
14. Section 3 of this report.
15. J.R. Fienup and C.C. Wackerman, "Phase retrieval stragration problems and solutions," *J. Opt. Soc. Am.* **A11** (1986) 1897.
16. M. Elbaum, private communication.
17. D. E. B. Lees, "Improved Autocorrelation Zero-Lag Estimation in Multiple Aperture Imaging Systems," *Active IRIS* (October, 1988).